



Turning Back the Clock on the Milky Way: Can We Observe Young Globular Clusters Forming at High Redshift?

Emma Dodd

MPhys Physics with Astrophysics and Cosmology
PHYS451 - Masters Thesis

April 2020

Abstract

Globular clusters (GCs) are old, dense, gravitationally bound groups of stars. They can be found throughout all components of the Milky Way and in galaxies of all morphologies. With age estimates on the order of the age of the Universe, they are thought to act as the building blocks for galaxy formation, providing us with fossils that we can study directly. Despite having been studied extensively, their own formation still remains a mystery, due to limited observations and an incomplete picture of their evolution. While potential young GCs have been identified at high redshift, it is difficult to determine whether these systems will in-fact evolve to resemble those seen in the Milky Way today. Therefore we attempt to backwards model six GCs and predict how they looked at formation and if they could be observed with Hubble. The measured properties of the six Milky Way GCs, including the most massive NGC 5139, are presented, determined from fitting isochrones to colour-magnitude diagrams constructed from archival Hubble images in filters: F438W, F606W and F814W. Age estimates for the clusters are of the range 10.5 to 12.5 Gyrs and metallicity estimates span -1.6 to -2.2 dex, with typical uncertainties of ± 2.0 Gyrs and ± 0.5 dex respectively. Thus confirming that globular clusters are old, metal-poor systems. Through modelling and accounting for mass loss, we produce images of the young GCs at the distance they are currently at and also at a redshift of 2.0 and 6.6, spanning the epoch of the Universe when these systems likely formed. We find that the young GCs at redshift $z = 2.0$ and 6.6 are too faint to be observable with a Hubble Ultra Deep Field (HUDF) like exposure. In reality many more dynamical processes result in mass loss from an evolving GC such that a young GC should be significantly more massive than today. Our simplistic models only take into account stellar evolutionary processes, finding a lower limit of the young GCs to be ~ 1.5 times more massive than today. However, they would need to be ~ 50 times more massive to be able to be observed with HUDF exposures at $z = 2.0$. With the upcoming JWST, observations of young GCs will be possible and will be vital for further constraining formation and evolution scenarios.

Acknowledgements

I would firstly like to thank my supervisor David Sobral, not only for the support and encouragement in my master's project, but for all four years here at Lancaster. For believing in me and my ability before I did myself, and for providing me with so many wonderful opportunities! I would not be where I am today without this.

I would also like to thank Alice Zocchi for introducing me to the world of globular clusters and teaching me so much while being patient with me as I learnt. I have fallen in love with globular clusters because of the passion and encouragement you showed to me.

I am extremely grateful to the Lancaster University Physics department, especially the observational astrophysics group, for making me feel so at home here. I have learnt a lot from every single member of staff in the group and appreciate all that you have taught me. I will be very sad to move on from this wonderful group.

Thank you to all of the PhD students in the office. It has been a wonderful place to work filled with so much support, helpful discussions and constant laughter. I hope that I will be as good a PhD student as all of you are. A huge thank you to Heather Wade for being a brilliant friend and daily inspiration. Thank you for running my scripts to generate the clusters for this thesis, when I could no longer access the astro-lab.

None of this would be possible without the continued support from my friends and family. Thank you to Eleanor D'Arcy for being my family at University and always encouraging me to be my best. Thank you to my Mum for teaching me to always reach for the stars. To my brothers, Nicholas and Dominic, for listening to me go on and on about globular clusters and making every day a laugh. To my sister for supporting me but also making sure that I take breaks and have fun. Finally, to my Dad, I hope that I will make you proud.

Contents

1	Introduction	1
1.1	Λ CDM Cosmology	1
1.2	Galaxy Formation	2
1.3	Globular Clusters and Galaxy Formation	2
1.3.1	The Milky Way System of Globular Clusters	3
1.4	Individual Globular Clusters	4
1.5	Progenitor Globular Clusters at High Redshift	5
1.6	This Study	6
2	Sample and Data	7
2.1	Selection of Milky Way Globular Clusters	7
2.2	Imaging Data	9
3	Using Observational Data	11
3.1	Constructing CMDs	11
3.1.1	Zero-Points	11
3.1.2	Producing Catalogues	12
3.2	Determining Cluster Properties	14
3.2.1	Dartmouth Stellar Evolution Database	15
3.2.2	Fitting Models	15
4	Observational Results	16
4.1	NGC 5139	17
4.2	NGC 3201	18
4.3	NGC 5466	19
4.4	NGC 6934	20
4.5	NGC 6441 and NGC 6624	21
5	Generating Clusters and Turning Back the Clock	21
5.1	Present-day Mass Functions	21
5.2	Initial Mass Functions	24
5.3	Mass-Temperature Relation	25
5.4	Black-body and Fluxes	27
5.4.1	Filter Profiles	28
5.5	Positions of Stars	29
5.5.1	Number of Stars	30
5.5.2	Magnitude Limit	30
5.6	Placing at High Redshift	31
5.7	Steps for Producing the Generated Images	34
6	Generated Results	34
7	Discussion	38
8	Summary	40

1 Introduction

1.1 Λ CDM Cosmology

The Universe is theorised to have formed through the Hot Big Bang model of cosmology 13.8 billion years ago (Aghanim et al., 2018). Currently, the standard cosmological model which provides the most detailed description of structure formation and has the most supporting evidence (e.g. the origin of the Cosmic Microwave Background Penzias & Wilson (1965)) is the Λ CDM model. Through this model, the Universe can be split into two separate components of energy density: a dominant dark energy component ($\sim 70\%$) and a matter component ($\sim 30\%$). The matter component of the Universe can be further split into a baryonic component consisting of normal matter ($< 5\%$) and the remaining to a dark matter component (Aghanim et al., 2018). A corresponds to the cosmological constant, which is proposed to cause the accelerated expansion of the early Universe. Currently, dark energy, the dominant component of the Universe, is the accepted form of the cosmological constant. CDM corresponds to cold dark matter, which is the non-relativistic and weakly interacting matter component of the Universe, first postulated by Peebles (1982) and later adopted into this model of structure formation by Blumenthal et al. (1984).

The first observational evidence of Big Bang cosmology comes from the discovery that the Universe is expanding (Hubble, 1929; Lemaitre, 1927). Tracing this expansion back agrees with a key part of Big Bang cosmology: that the Universe started from an initial dense singularity. The discovery of an expanding Universe arose from accurate measurements of galaxy's distances and recessional velocities, leading to the Hubble-Lemaitre Law that revolutionised our understanding of cosmology.

Cosmological redshift is a result of this expanding Universe and is an important quantity for studying distant galaxies. As the Universe expands and the space in-between galaxies grows, the wavelength of the light emitted from a distant galaxy is stretched. The further away the galaxy is, the longer the wavelength of light is stretched by and the higher the redshift of this galaxy, according to,

$$z = \frac{\lambda_o - \lambda_e}{\lambda_e} \quad (1.1)$$

where λ_o is the observed wavelength and λ_e the rest-frame emitted wavelength. The scale factor, $a(t)$, is another measure of the expansion of the Universe and is related to redshift as follows,

$$\frac{a(t_o)}{a(t_e)} = 1 + z \quad (1.2)$$

where $a(t_o)$ corresponds to the size of the Universe at the time when the light is observed and $a(t_e)$ to the size of the Universe at the time when the light from the galaxy was emitted. A redshift of 1 corresponds to a Universe that was half the size of today.

Distances in the Universe are vast, such that it takes the light emitted from a distant galaxy a very long time to reach us. Since light travels at one set speed, $c \sim 3 \times 10^8 \text{ ms}^{-1}$, the further away a galaxy is, the longer it takes for the light to reach us. Therefore, through observations, we see how the galaxy looked when this light was emitted. A higher redshift corresponds to a more distant source and therefore a longer light travel time, and hence corresponds to an earlier epoch of cosmic time. Quantitatively, redshift scales logarithmically with the age of the Universe such that a $z = 0.1$ corresponds to a light travel time of 1.3 Gyrs and a Universe that is 12.2 Gyrs old. A redshift, z , of 1 to a light travel time of 7.7 Gyrs and a Universe that is 5.7 Gyrs old and $z = 10$ to a light travel time of 13.0 Gyrs and a Universe that is only 0.5 Gyrs old¹ (Wright, 2006).

¹Calculated assuming a flat Universe with $H_0 = 70 \text{ km s}^{-1} \text{ Mpc}^{-1}$, $\Omega_M = 0.3$ and $\Omega_\Lambda = 0.7$.

Expansion was vital for allowing the early Universe to cool and begin to form the structure that we see today. Once the Universe had cooled enough for electrons and protons to combine the Cosmic Microwave Background (CMB) was emitted. Temperature fluctuations in the CMB led to density perturbations, which were then able to grow during the inflation period of cosmic history (Guth, 1981). These density perturbations gave rise to dark matter haloes which seeded structure formation as they formed potential wells to trap gas. As the Universe continued to expand, it then cooled down enough for the gas to collapse gravitationally such that stars and galaxies could begin to form (Guo et al., 2010).

With the formation of the first structures, the Universe then entered a phase called the epoch of reionisation, in which the neutral Universe was ionised. The timeline of this is still uncertain but is believed to have come to an end by $z \sim 6$ (e.g. McGreer et al., 2015). It is also not yet clear which sources in the early Universe were responsible for powering this reionisation. One possible contributor is the theorised first generation (Population III) stars (e.g. in high z galaxies like CR7, Sobral et al., 2015). Another potential contributor is globular clusters, due to their old ages they are predicted to form at high redshifts spanning the epoch of reionisation phase. The large numbers of these systems present around almost all galaxies and rapid star formation timescales mean that they could be a dominant contribution to the reionisation of the Universe (Boylan-Kolchin, 2018).

1.2 Galaxy Formation

Galaxy formation can be considered to consist of two separate phases (Oser et al., 2010). The first ‘in-situ’ phase, occurring at high z in the early Universe, builds up the centres of galaxies forming stars from cooling gas collapsing within dark matter haloes. Secondly, the ‘ex-situ’ phase, occurs over the rest of the galaxy’s lifetime as smaller bodies, including low mass galaxies, are accreted building up a more massive galaxy halo. It is thought that all galaxies begin as disk galaxies, forming by the in-situ phase, but the growth into more massive disk galaxies (e.g. like our own, the Milky Way) and the formation of all other morphologies (e.g. ellipticals) are proposed to have formed ex-situ, through interactions and merger events. This theory is supported by both observations (e.g. Toomre et al., 1977) and simulations (e.g. Steinmetz & Navarro, 2002).

Understanding the formation and evolution of galaxies is a major challenge that requires a variety of approaches to tackle. The first step in this direction is to try to understand how our galaxy (the Milky Way) formed, owing to the accessibility to study individual stars and the large wealth of data we already have of our galaxy. The Milky Way is a spiral type galaxy. It is made up of several components, the central bulge and bar (that likely formed first through in-situ processes), a disk with ongoing star formation (which can be subdivided into a thin and thick disk with different origins) and a Galactic halo that consists of older stars. There is also a dark matter halo that surrounds the galaxy, like all other galaxies. The different components are theorised to have formed at different times and via a range of processes (see recent review by Helmi, 2020). Globular clusters (GCs) in the Milky Way are distributed throughout all of these different components of the galaxy and thus are one key tool for unveiling the formation history of our entire galaxy.

1.3 Globular Clusters and Galaxy Formation

Globular clusters are old, dense, gravitationally bound clusters of 10^5 - 10^6 (Stetson et al., 1996) stars held together in an approximately spherical distribution. They are the oldest stellar clusters known with ages ranging from a lower limit of ~ 10.5 Gyrs (VandenBerg et al., 2013) to an upper limit of ≤ 13.5 Gyrs (Jimenez, 1998). Thus providing an estimate for the minimum age of the Universe. These stellar systems, which are present in almost all galaxies, are extremely useful fossils of the early Universe, that we can study directly. However, there is still a lot of uncertainty surrounding globular cluster formation. Due to the majoritively old ages of these

systems we know that most formed at high redshift, when the Universe was significantly younger, and as such observations of individual stellar clusters are limited, see Section 1.5 for more detail. Despite the difficulties associated with observations, understanding GC formation is a vital step for constraining models of the Milky Way's formation.

Currently, there are three different classes of GC formation; primary, secondary and tertiary which correspond to whether GCs formed before, with or after the formation of the host galaxy Fall & Rees (1988). It is most likely that the formation of GCs throughout the entire history of the Universe belongs to more than one of these classes. As mentioned previously, galaxy formation is a two-stage process that involves both in-situ and ex-situ processes. Observations of the GC systems in our own galaxy supports this theory (e.g. Myeong et al., 2019; Massari et al., 2019; Forbes, 2020), along with simulations of merger interactions (e.g. Kruijssen, 2014). It is predicted that along with GCs accreted from the other galaxy during a merger event, a new population of GCs can also form during this violent process (Ashman & Zepf, 1992). This suggests that GC formation happens not only at high redshift but also at this epoch in interacting galaxies. The conditions in a significant merger interaction (starburst) appear to match those at high redshift that are necessary for GC formation, with simulations in agreement (e.g. Bournaud et al., 2008). However, both observations and more in-depth models of the conditions for GC formation are needed to explore this further. Currently, observations of star cluster formation is challenging, as during the early stages of their life they remain embedded in large clouds of interstellar gas and dust. It is hoped that this may become possible with infra-red imaging on JWST. There are also limitations in that there is not yet an established picture of how GCs looked when they first formed as this requires sophisticated backwards modelling.

1.3.1 The Milky Way System of Globular Clusters

The Milky Way contains ~ 150 confirmed globular clusters. To date, the most extensive catalogue of their properties is that of Harris (1996). It has been suggested that the true amount of GCs in our galaxy is actually ~ 180 , but these that remain to be discovered are likely obscured by the Galactic bulge and as such prove difficult to observe (Ashman & Zepf, 2008).

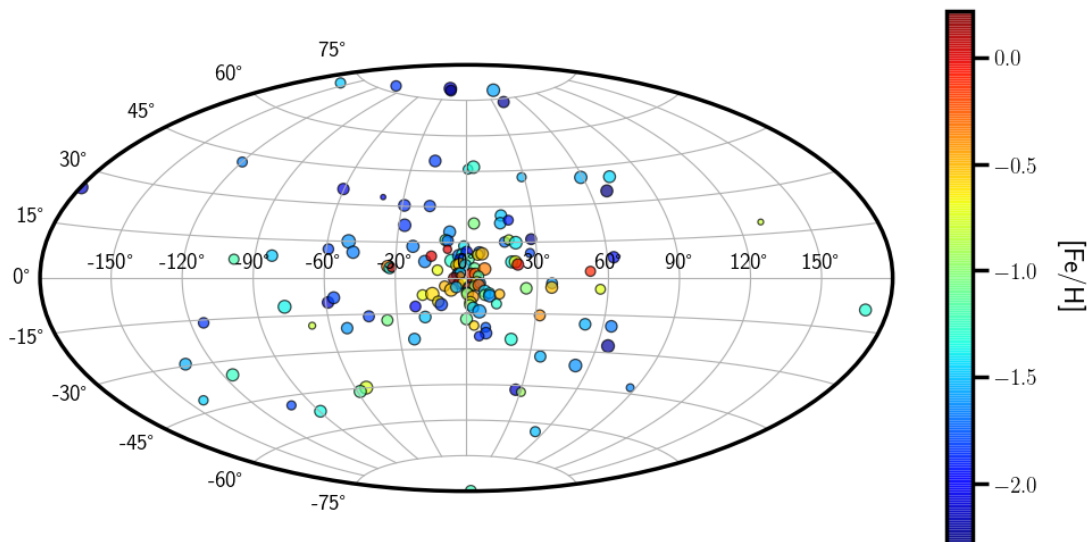


Figure 1: Spatial distribution of Harris (1996) Milky Way globular clusters colour-coded by metallicity and size scaled by the V band magnitude of the cluster. Two distinct populations can clearly be seen; a metal-rich central population and a more extended metal-poor population, associated with the halo.

According to the theories of galaxy formation, the Milky Way should contain both GCs formed in-situ and those formed ex-situ. The metallicity gradient observed in the Milky Way GC system,

shown in Figure 1, supports this. There are two distinct populations of globular clusters in the Milky Way, split both spatially and in metallicity. The metal-rich centrally concentrated population is thought to have formed in-situ, and the metal-poor population are likely accreted. Current studies are underway to identify the progenitor galaxies that the accreted GCs came from, (e.g. [Myeong et al., 2019](#); [Massari et al., 2019](#); [Forbes, 2020](#)) finding that of the ~ 150 GCs a significant fraction (50-60%) were formed ex-situ and later accreted. More accurate measurements of the chemical properties of Galactic GCs, along with the next GAIA data release should significantly advance the determination of which GCs came from which progenitor galaxies.

1.4 Individual Globular Clusters

As a system, globular clusters are extremely useful for furthering our understanding of the Milky Way's formation and evolution history. Individually they are perfect examples and tests for stellar evolution models. It was originally assumed that GCs formed rapidly (over \sim few Myrs) in a single massive burst of star formation from one large gas cloud and thus all stars should have very similar properties, e.g. age and metallicity ([Beasley, 2020](#)). This coeval group of stars with the same chemical composition is known as a simple stellar population (SSP) (see [Bruzual A, 2010](#), for a review of star clusters as SSPs).

Stars are classified according to their temperature by the Harvard Classification of spectral type. The order of spectral type, OBAFGKM, is of decreasing surface temperature which controls the strength of the absorption lines in spectra ([Morgan & Keenan, 1973](#)). Luminosity and temperature of a star depends on mass, age and chemical composition. Since for a SSP, all stars have the same age and chemical makeup, the main factor that derives differences between the evolutionary stage of each star in the population is the initial mass. Therefore the different spectral types in GCs can be considered to be stars of different masses, with O type being the most massive.

Since all stars in a GC are thought to have formed within a few Myrs, there will be a time when all the stars will be in the main-sequence phase of their life, burning hydrogen into helium in their core via nuclear fusion. The most massive stars, however, will use up their fuel faster and thus have shorter main-sequence lifetimes. The main-sequence (MS) lifetime of the most massive star still on MS in a GC today will give a lower limit for the age of the cluster ([Chaboyer, 2001](#)). Once a star leaves the main-sequence it enters the red giant branch phase, fusing helium to produce all heavier elements, commonly called metals². The next stage of evolution is determined by the initial mass of the star. High mass stars ($> 8M_{\odot}$) will go supernova and enrich the surroundings with the metals that have been produced in the core, leaving a compact neutron star or black hole behind ([Heger et al., 2003](#)). However, low mass stars ($< 8M_{\odot}$) do not go supernova and the metals produced in the core remain locked up in white dwarf remnants ([Weidemann & Koester, 1983](#)). Stellar remnants in GCs are difficult to observe due to overcrowding and are the subject of many studies to date, e.g. see [Steiner et al. \(2018\)](#) for neutron stars in GCs, [Giesers et al. \(2018\)](#) for observations of a stellar mass black hole in Milky Way GC NGC 3201 and [Kremer et al. \(2018\)](#) for modelling of GCs with stellar mass black holes. This will be discussed further in Section 5.1.

Since the stars in Milky Way GCs are old, they formed when the Universe was younger and before it had been enriched by many previous generations of stars, hence why they are metal-poor. GCs are made up of what is known as the second generation of stars (Population II). Metallicity of a star can be sometimes used as a tracer of age. The age-metallicity relation for Milky Way globular clusters has been observed to be split, signifying different origins (in-situ and ex-situ) for the two populations of GCs (e.g. [Leaman et al., 2013](#)).

²The fusion of hydrogen and helium in the cores of the first generation of stars is what produced all of the heavier elements present in the Universe today.

One key tool for tracking the stellar evolution of SSPs is to use colour-magnitude diagrams (CMDs). These diagrams make use of the relation of the colour of a star to the surface temperature and luminosity to absolute magnitude. Where a star lies in a CMD is dictated by mass, age and chemistry, and so for a simple stellar population, it is solely determined by the mass of the star. The most populated regions of CMDs are where a star spends the majority of its life, e.g. the main-sequence, where a star spends $\sim 90\%$ of its life. A GCs CMD includes stars in all possible phases of stellar evolution, which is what makes them so useful for understanding more about stellar evolution and testing these models.

Observed CMDs of globular clusters can be used to determine the properties of the cluster, see [Sandage \(1953\)](#) for Milky Way example and [Ma et al. \(2010\)](#) for Andromeda (Local Group galaxy) example. The main-sequence turn-off point (MSTO) shifts to fainter magnitudes and redder colours for older stellar populations, and thus is the key feature of CMDs for determining the ages of clusters ([Chaboyer, 2001](#)). Following the main-sequence phase, older stars begin to populate the horizontal branch (HB), where helium is now being fused in the core. Metallicity of the stellar population significantly influences the morphology of the horizontal branch, along with small influences from other properties such as age (see e.g. [Recio-Blanco et al., 2006](#), for more information on what is known as the second parameter problem). All GCs observed horizontal branches have a RR Lyrae gap, corresponding to the population II variable stars typically observed in clusters ([Clement et al., 2001](#)). Stars in the observed CMD of a SSP can be represented with a single isochrone; a theoretical stellar evolutionary track consisting of a population of stars according to an initial mass function, with all stars of a given age and metallicity. The best-fit isochrone to the observed CMD thus gives the best-fit properties for the GC ([Dotter et al., 2007](#)).

It is now known that GCs are not made of only one simple stellar population but in-fact contain multiple populations (e.g. see review by [Gratton et al., 2012](#)). This phenomenon was first found in the more massive GCs (e.g. ω Centauri [Bedin et al., 2004](#)) and later confirmed to be a property of all GCs, at least those in the Milky Way ([Piotto et al., 2012; Milone et al., 2017](#)). However, for the purpose of observing young GCs at high redshift, we can assume that GCs can be represented as a coeval population. Although it was once theorised that these multiple populations could be explained by inhomogeneities in the original material in which the GC formed from, (see e.g. review by [Kraft, 1979](#)), this is not significant enough to explain the spread in age and metallicity seen in the majority of GCs. Therefore multiple populations are thought to have instead arisen over a clusters lifetime, produced during a second (and successive) round(s) of star formation triggered through different scenarios. For example, through the merging of globular clusters (see [Calamida et al., 2020](#), who find support for the merger scenario formation of ω Cen's multiple populations) or accretion of interstellar matter through interactions with star-forming clumps (modelled by [Bekki & Mackey, 2009](#)). Most stars in GCs today are of this second (and successive) generation(s) of star formation, with only around one third belonging to the original stellar population produced during the birth of the cluster ([Gratton et al., 2012](#)). GCs that have just formed, however, will only contain the original generation and can be modelled relatively successfully as a SSP. When looking at young GCs we are looking at the first few Myrs of the clusters life, on timescales shorter than the evolutionary timescales for massive stars, and therefore likely before any significant variations due to multiple populations could have arisen.

1.5 Progenitor Globular Clusters at High Redshift

The minimum age of Milky Way globular clusters, ~ 10.5 Gyrs ([VandenBerg et al., 2013](#)), suggests that all must have formed at redshifts $z > 2$ ([Wright, 2006](#)). Therefore it seems possible that we may be able to witness GC formation through observations at high redshift. Studies have attempted to estimate the number of GC progenitors that will be present in the Early Universe, e.g. [Renzini](#)

(2017) predict that, assuming a constant formation rate of GCs from $z = 3 - 10$, at least 200,000 of these progenitors should be included in one single frame of NIRCam on JWST. Following this, [Pozzetti et al. \(2019\)](#) model the expected properties of progenitor GCs at high z , finding that the number that can be observed depends critically on how massive they were at formation. The ratio of initial mass to the present-day mass of a GC is known as the mass budget factor, which is crucial for determining how many progenitors can be observed. For a mass budget factor of 1 only 10 progenitors can be detected with NIRCam, but with a factor of 10 then 1000 progenitors could be observed with a limiting magnitude of ~ 30 ([Pozzetti et al., 2019](#)). The value of the mass budget factor of GCs is still under debate as many factors influence the loss of cluster mass over its lifetime. Mass loss due to stellar evolutionary processes, e.g. stellar winds, is thought to only account for a factor of ~ 1.7 ([Pozzetti et al., 2019](#)), whereas models that take into account dynamical processes, such as evaporation, suggests this factor could be as high as 10 for some clusters, with an average of ~ 4.5 ([Webb & Leigh, 2015](#)). The number of progenitors that JWST is able to identify once it launches will provide observational constraints on the mass budget factor and further constraints on modelling the formation and evolution of GCs ([Pozzetti et al., 2019](#)).

Before JWST, however, young GCs could already in-fact be visible in archival deep images. [Vanzella et al. \(2017\)](#) conducted a study using MUSE/VLT and the Hubble Frontier Field (HFF) to look at gravitational lensed faint compact sources at high redshift and found two potential progenitor GCs with properties similar to what is expected of forming GCs. [Bouwens et al. \(2017\)](#) also observe the HFF utilising gravitational lensing to detect 307 faint sources from $z = 6 - 8$. A small number of these are consistent with that of progenitor GCs, resembling super star clusters with sizes and masses that are consistent with small multiples of today's GCs. More recently, [Kikuchi et al. \(2019\)](#) extend this study of faint objects to include the entirety of the HFF fields using the deep images available. They find two objects with masses and sizes in agreement with the upper limits of GCs that exist today. Potentially more of the observed sources could be considered to be potential young GCs if acknowledging that GCs were possibly much more massive at formation. However, further constraints on the mass budget factor are needed first. The majority of observations to date have been aided with the use of gravitational lensing to be able to detect the faint sources at high z with Hubble. It is likely that we will be unable to make any confirmations between a young GC or proto-galaxy at high redshift, since they have similar sizes and masses, until we are able to resolve these objects better, possibly with JWST.

One attempt for confirming potential progenitor GCs is through comparison of these observations with cosmological simulations of forming GCs. For example [Phipps et al. \(2019\)](#) utilise the First Billion Years cosmological simulations to investigate young globular clusters, studying the sizes, masses and environments of the candidates. The young GCs appear to be more extended than typical present-day GCs, and comparisons with the previous observations from [Vanzella et al. \(2017\)](#) and [Bouwens et al. \(2017\)](#) appear to be consistent.

1.6 This Study

Difficulties still arise in knowing whether these observed progenitor GCs at high z will in-fact evolve into resembling a GC like that of the Milky Way today. Therefore, we attempt to backwards model a handful of Milky Way globular clusters to obtain an idea of how these systems looked when they were young. These young globular clusters can then be placed at high z to see if we are able to observe them today with deep imaging such as the Hubble Ultra Deep Field (HUDF) ([Beckwith et al., 2006](#)) and to see of any similarities between previous observations of potential progenitor GCs.

This thesis is structured into two main parts; determining the properties of a selection of Milky Way GCs and generating young GCs to place at high z . Firstly, Section 2 outlines the chosen

Milky Way GCs for this study and the corresponding Hubble data used. Section 3 outlines the methods taken for producing stellar catalogues from this data for CMDs and then determining cluster properties from fitting isochrones to the constructed CMDs. Section 4 briefly outlines the first set of results in this thesis: the measured properties for our chosen sample of Milky Way GCs. These results are then used for generating our young GCs through the adoption of stellar models and assumptions, outlined in Section 5. Generated clusters are then shown in Section 6 and all results discussed further in Section 7.

2 Sample and Data

2.1 Selection of Milky Way Globular Clusters

For this study, a handful of Milky Way globular clusters were selected to be investigated for the initial stages of the project, determining globular cluster properties. The clusters were selected based on the Hubble Space Telescope (HST) data available in the required filters and detectors, discussed further in Section 2.2, and also such that the sample of globular clusters represents the entire Milky Way population. Figure 2 shows the spatial distribution of 147 of the Milky Way globular clusters, from the [Harris \(1996\)](#) catalogue, with those selected for this study highlighted. Six globular clusters have been selected to represent the different regions of the Milky Way, the bulge and both the inner and outer halo globular clusters. This way, it can be seen how globular clusters from different regions of the Milky Way looked at their time of formation and whether there are any obvious differences.

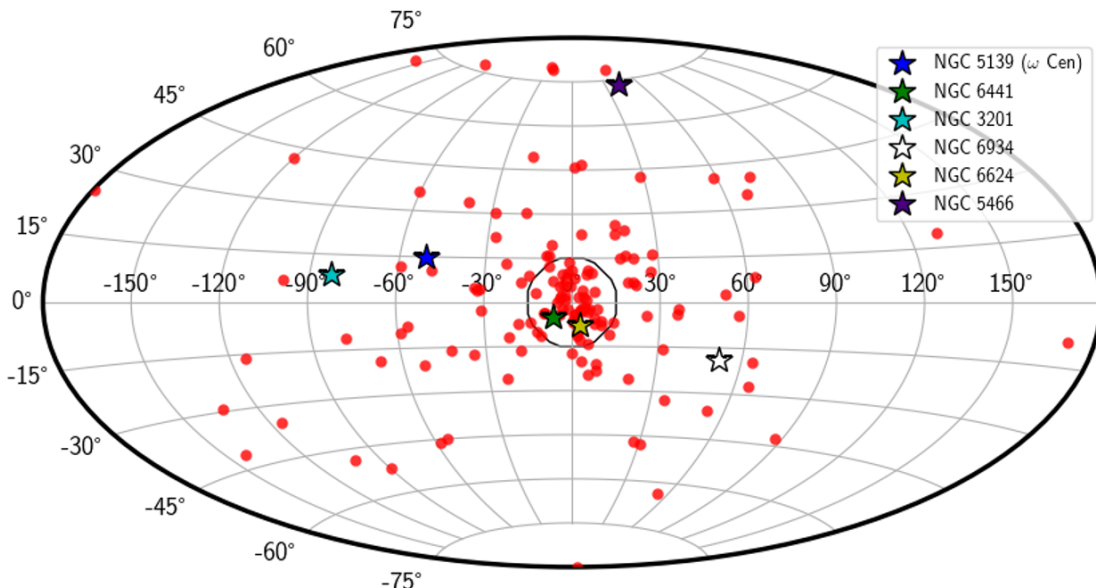


Figure 2: Spatial distributions of globular clusters belonging in the Milky Way with globular clusters that have been chosen for this study highlighted with star markers. The circle at 15° corresponds to how far the bulge extends ([Zinn, 1996](#)). This figure was made using the [Harris \(1996\)](#) catalogue of Milky Way globular clusters.

The sample was also chosen to represent the wide range of properties that have been observed for Milky Way globular clusters. While we know that all globular clusters are old, with age estimates of e.g. 10 - 16 Gyrs ([Krauss & Chaboyer, 2003](#)), and metal-poor, with [Fe/H] estimates of e.g. -0.3 to -2.4 dex ([Carretta et al., 2009](#)), they are so by varying degrees. Our chosen sample represents the spread in these properties, as demonstrated in Figure 3. The clusters chosen are varied in all of the following: central concentration, metallicity, absolute magnitude and age. Thus representing the

spread of these parameters across the entire Milky Way. Table 1 shows the averages of the different cluster properties represented by our chosen sample, which reflect that of the entire [Harris \(1996\)](#) sample.

The first panel of Figure 3 shows the spread in concentration parameter, c , which is calculated as

$$c = \log\left(\frac{R_t}{R_c}\right) \quad (2.1)$$

where R_t is the tidal radius and R_c the core radius of the cluster. In the second panel we see the range of metallicities for the sample. Metallicity is commonly denoted $[\text{Fe}/\text{H}]$, which is defined as

$$[\text{Fe}/\text{H}] = \log\left(\frac{N_{\text{Fe}}}{N_{\text{H}}}\right)_{\text{star}} - \log\left(\frac{N_{\text{Fe}}}{N_{\text{H}}}\right)_{\text{sun}} \quad (2.2)$$

where N_{Fe} and N_{H} are the number of iron and hydrogen atoms per unit volume. Next, the third panel of Figure 3 shows the average ages of our globular clusters, taken from [Kharchenko et al. \(2016\)](#), and finally, the last panel shows the spread in absolute magnitude of the sample of clusters. It can be seen that the ages of these clusters are all very similar, and the age spread very minimal. This means that the magnitude of a cluster can link directly to the mass and size.

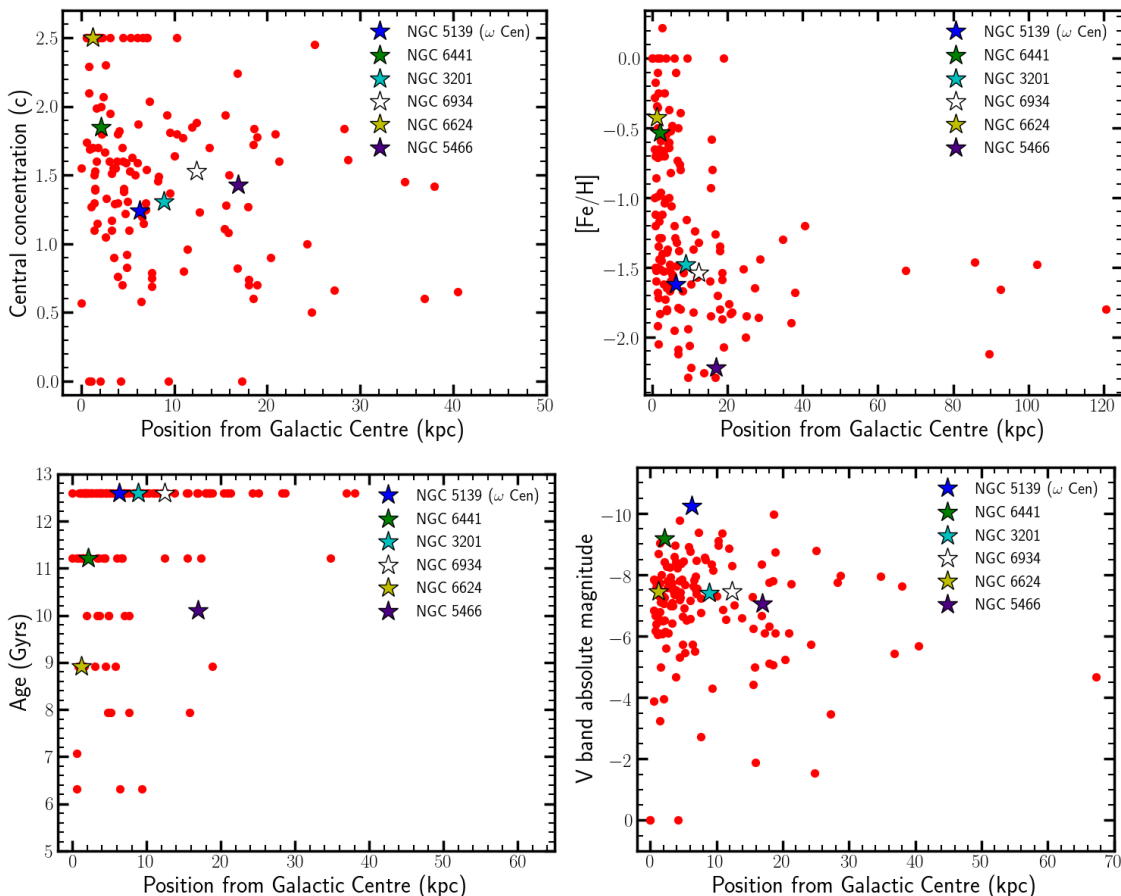


Figure 3: Varied parameters of the chosen GCs compared with the entire sample of Milky Way globular clusters. Concentration, $[\text{Fe}/\text{H}]$ and V band magnitude data all taken from [Harris \(1996\)](#), and ages taken from [Kharchenko et al. \(2016\)](#).

We are looking at the more massive globular clusters in the Milky Way when we are looking at those with a lower absolute magnitude (lower magnitude corresponds to a brighter cluster). NGC 5139, more commonly known as ω Centauri, has the lowest absolute magnitude and is the most

massive globular cluster in the Milky Way (e.g. see [Gnedin et al., 2002](#)). There are many reasons for why this cluster has been chosen in our sample. Firstly, since it is the most massive, it is one of the best studied of the GCs in our galaxy, and therefore comes with a wealth of available data and results for comparison. It is also important because when observing young clusters at high redshift, we will be bias to the most massive, due to observing limits. Therefore, the most massive young clusters will likely evolve into the most massive globular clusters today, if they are progenitor globular clusters. By comparing the more massive GCs today, like ω Centauri for one, we are comparing like with like and taking into account this observing bias at high redshift.

Sample	R_{Sun} (kpc)	R_{GC} (kpc)	$E(B-V)$	Age (Gyrs)	M_V	[Fe/H] (dex)	c
Harris (1996)	15	12	0.5	10.3	-6.9	-1.2	1.5
This Study	10	8	0.2	10.2	-8.1	-1.3	1.6

Table 1: Table comparing the mean value for various parameters of our chosen sample of clusters to the whole [Harris \(1996\)](#) sample, where R_{Sun} is the distance to the Sun and R_{GC} the distance to the Galactic centre.

2.2 Imaging Data

In order to measure the properties of our sample of globular clusters from constructed colour-magnitude diagrams, stellar catalogues were needed in two filters. The catalogues of stellar magnitudes in the two chosen filters were used to obtain a colour index for the stars in the cluster, which is discussed further in Section 3.1. Image data in different filters was needed to obtain our stellar catalogues. For this study HST data has been retrieved from the archive in the relevant filters. Since the filters chosen will determine the colour index of the stars, the standard approach of $B - V$ was chosen. HST filters that correspond to B and V which are used on the ACS (Advanced Camera for Surveys) and WFC3 (Wide Field Camera 3) are F606W and F438W commonly described as Wide Johnson V and Johnson B respectively (e.g. in [Bellini et al., 2017a](#)). ACS and WFC3 are the detectors used in this study. Data was also collected in a third filter in the infra-red, F814W, in-case of use for the stellar catalogues (F814W - F606W instead of F606W - F438W for colour index) and for the creation of RGB images in which case three filters are necessary. Table 2 shows the data collected for use in this study with the filter, proposal ID and detector. Data has been collected from three different proposals: 10775, 13297 and 11911.

Firstly, proposal 10775 ‘*An ACS Survey of Galactic Globular Clusters*’ was specifically designed for improving the photometry available for Milky Way globular clusters and for determining properties including from the use of colour-magnitude diagrams ([Sarajedini, 2005](#)). Included in this proposal are filters F606W and F814W. This survey is a HST treasury project and contains data for 65 GCs in the Milky Way, including for some clusters that had no previous HST image data, e.g. NGC 5466 which is one of the clusters chosen for this study ([Sarajedini et al., 2006](#)). This proposal has been useful for advances in many areas of the field including but not limited to: accurately determining the centres of Galactic GCs ([Goldsbury et al., 2010](#)), unveiling properties of GCs in the bulge of the Milky Way ([Alonso-García et al., 2012](#)) and understanding further the formation history of globular clusters with respect to the formation of the halo from the calculation of relative ages ([Marin-Franch et al., 2009](#)). The second paper in the ‘*An ACS Survey of Galactic Globular Clusters*’ series, ([Dotter et al., 2007](#)), presents a set of stellar evolutionary tracks (isochrones) for use in analysing this image data. This library was then extended further to encompass a larger range in parameters giving rise to the *Dartmouth Stellar Evolution Database*, revolutionising the field and what can be learnt about globular clusters, without which this work would not be possible ([Dotter et al., 2008](#)). This database and the isochrones are discussed further in Section 3.2.1.

Secondly, proposal 13297 ‘*The HST Legacy Survey of Galactic Globular Clusters: Shedding UV Light on Their Populations and Formation*’ was later carried out as an extension to 10775 in order to image the Galactic globular clusters in more filters, including UV and blue filters such as F438W which is crucial for this work (Piotto, 2013). The extension of filters is necessary for determining properties such as detecting multiple populations through CNO abundance variations between first and second generation stars in globular clusters, which these extra filters (mainly F275W, F336W, F438W) are more sensitive to (Piotto et al., 2015) and also for alternative identification methods of blue straggler populations in globular clusters using UV bands (Raso et al., 2017).

Name	Filter	Proposal ID	Detector
NGC 5139	F438W	11911	WFC3
	F606W	11911	WFC3
	F814W	11911	WFC3
NGC 6441	F438W	13297	WFC3
	F606W	10775	ACS
	F814W	10775	ACS
NGC 5466	F438W	13297	WFC3
	F606W	10775	ACS
	F814W	10775	ACS
NGC 3201	F438W	13297	WFC3
	F606W	10775	ACS
	F814W	10775	ACS
NGC 6934	F438W	13297	WFC3
	F606W	10775	ACS
	F814W	10775	ACS
NGC 6624	F438W	13297	WFC3
	F606W	10775	ACS
	F814W	13297	ACS

Table 2: Hubble Space Telescope (HST) data used in this study for the six Milky Way globular clusters in the sample showing the filters collected, corresponding proposal ID and the detector used.

While there is data for NGC 5139 in proposal 10775, both in F606W and F814W, this cluster was unfortunately not included in the follow-up survey, proposal 13297. Therefore data for this cluster in F438W is missing, at least in the same region of the cluster as the imaged in 10775, and so we would not be able to produce matched stellar catalogues between these two filters. In order to be consistent and use the same colour index for all clusters, a different proposal was needed that included data for NGC 5139 in all of F438W, F606W and F814W, looking at the same regions. Luckily for ω Centauri there is a large abundance of data available from other proposals since it is the most massive globular cluster in the galaxy it has been very well studied (e.g. see Bellini et al., 2017a, for an outline of all of the WFC3 UVIS/IR archival data for the core of NGC 5139.) Data from proposal 11911 ‘*UVIS L-Flats and Geometric Distortion*’ was chosen for this study. Although this data was taken for the use of providing corrections for the WFC3/UVIS detector through the calculation of the geometric distortion, it provides high quality deep images of the core of NGC 5139 that are useful for this study (Sabbi, 2009). This proposal has been key in providing new results for NGC 5139 that have added to the discussion of a wide range of open questions including multiple populations in GCs (Bellini et al., 2017c), blue straggler identification in GCs (Baldwin et al., 2016) and adding to the HSTPROMO (Hubble Space Telescope Proper Motion) catalogue of Galactic globular clusters by determining the proper motions of NGC 5139 members (Bellini et al., 2014).

3 Using Observational Data

This section presents the first stages of the project which involved using the image data, presented in Section 2.2, to produce stellar catalogues and colour-magnitude diagrams for each cluster with the goal to determine their properties from the fitting of stellar isochrones.

3.1 Constructing CMDs

Source-Extractor, hereafter referred to as **SExtractor**, is a software used to obtain the photometry and position of each star in an astronomical image ([Bertin & Arnouts, 1996](#)). The first steps in constructing a CMD for each of the chosen globular clusters in the sample is to produce a stellar catalogue of sources in the different filters. This was done using **SExtractor** on the HST images for each cluster to produce catalogues for each filter.

3.1.1 Zero-Points

Several parameters are needed for **SExtractor** to be able to measure the photometry of stars accurately. Astronomical images are made up of the value of the number of counts for each pixel which can be converted into a magnitude for a source when averaging over a certain number of pixels. In order for **SExtractor** to convert that measured from the image into a magnitude for a source, the zero-point (ZP) of the image is needed. The ZP is defined by the detector and also the exposure time of the image. The apparent magnitude of a star (m) is calculated from the number of counts (c) and exposure time (t_{exp}) by the equation:

$$m = -2.5 \log\left(\frac{c}{t_{\text{exp}}}\right) + ZP_{\text{detector}} \quad (3.1)$$

where ZP_{detector} is the zero-point of the detector. Counts (c) is measured for a source in a specified aperture for images with units of electrons, in which case the ZP given to **SExtractor** must also include the exposure time for the specific image. In this case the ZP is given by the equation:

$$ZP = ZP_{\text{detector}} + 2.5 \log(t_{\text{exp}}) \quad (3.2)$$

such that:

$$m = -2.5 \log(c) + 2.5 \log(t_{\text{exp}}) + ZP_{\text{detector}} \quad (3.3)$$

$$m = -2.5 \log(c) + ZP \quad (3.4)$$

However, some of the data in the sample is already in units of electrons s^{-1} and so has already been corrected for the exposure time. In which case the ZP given to **SExtractor** is simply ZP_{detector} .

Cluster	Exposure Time (s)		ZP (AB mag)		Pixel Scale (''/pix)	
	F606W	F438W	F606W	F438W	F606W	F438W
NGC 3201	5	68	26.51	24.83	0.05	0.04
NGC 5466	4324	139	26.49	24.83	0.05	0.04
NGC 5139	360	3150	26.08	24.83	0.04	0.04
NGC 6934	45	64	26.51	24.83	0.05	0.04
NGC 6441	340	128	32.83 ¹	24.83	0.05	0.04
NGC 6624	350	62	32.87 ¹	24.83	0.05	0.04

Table 3: Exposure times and ZPs of images in the two filters used for CMDs for each cluster. NGC 6441 and NGC 6624 in F606W [1] corresponds to the images with units of electrons such that the ZP has been corrected for exposure time using ZP_{ACS} .

Values for ZP_{detector} for the different detectors and filters were taken from the literature with all images in F438W from WFC3 and images in F606W from either ACS or WFC3. In the study for ACS

we adopt $ZP_{ACS}(F606W) = 26.49$ ([De Marchi et al., 2004](#)) or 26.51 depending on the date of observation (checked through calculations with [STScI, 2020](#)). For WFC3 we adopt $ZP_{WFC3}(F606W) = 26.08$ and $ZP_{WFC3}(F438W) = 24.83$ ([Kalirai et al., 2009](#)). The specific zero-points used for each image of each cluster is summarised in Table 3 including those with t_{exp} corrections, with all magnitudes in the AB system. Also included in Table 3 is the pixel scales for WFC3/UVIS (0.04) and ACS/WFC (0.05) that are also necessary for choosing the aperture size when using **SExtractor** ([STScI, 2019](#)).

3.1.2 Producing Catalogues

Once the images had been corrected for the ZP, then a catalogue of stars for each image could be produced including AB magnitudes and positions of all sources. The magnitude is measured using **SExtractor** through an aperture of a selected size. It is important to make sure the size of the aperture used is greater than the seeing of the observational images. For example, if the images were observed from ground based telescopes where the typical seeing is $\sim 1''$ then using an aperture size of $1''$ will not be sufficient as individual sources can not be resolved this far. However, since we are using HST data this is not an issue, with a spatial resolution of $0.07 - 0.15''$ for WFC3 and ACS, we can resolve individual sources down to much lower levels ([Windhorst et al., 2011](#)). **SExtractor** also has the option to use Mag-Auto in which the total magnitude of a source is estimated by looking at how far a source extends using where the flux stops. This will give us the best estimate of each sources magnitude and so has been chosen to be used for the CMDs. The $1''$ aperture magnitudes are also included in the catalogue for completeness and comparison to make sure that Mag-Auto is estimating the total magnitude correctly.

Cluster	No of Sources		
	F438W	F606W	Matched
NGC 3201	10,177	8,705	5,212
NGC 5466	14,837	13,272	6,282
NGC 5139	120,733	103,650	75,898
NGC 6934	17,160	24,498	10,997
NGC 6441	38,286	44,403	21,242
NGC 6624	16,953	23,177	9,540

Table 4: Number of sources detected in both the F438W and F606W images, along with the sources matched between filters with a $1''$ tolerance for each cluster.

Once the catalogues had been produced for the images of each cluster in F438W and F606W, the two needed to be matched such that we had a final catalogue of stars in the cluster with magnitudes in both filters. Sources were matched in RA and Dec with a 1 arc-second tolerance to allow for slight misalignments in astrometry between filters using software designed specifically for dealing with astronomical data, TOPCAT ([Taylor, 2005](#)). Matching sources between the two filters should clean the individual catalogues of fake sources that arise due to noise, as they are unlikely to appear in both filters. The number of sources in the final matched catalogue, shown in Table 4, is reduced but contains a higher proportion of sources that we deem as real. There are more sophisticated methods that can be used for cleaning catalogues and determining cluster membership (e.g. see [Anderson et al., 2008](#)). Cleaning the catalogue is beyond the scope of this report, as individual stars are not important, only the structures they present in the CMD which can be used for determining the properties of the globular clusters.

Figure 4 shows one of the first CMDs constructed in this study. This is for NGC 5139 and is the catalogue that contains the largest number of sources. A clear main-sequence can be seen in this data with a sharp main-sequence turn-off point (MSTO) onto the red giant branch (RGB). The wings of the main-sequence are densely populated, likely due to noise, and is a reflection of that

the catalogue has not been cleaned properly (see e.g. [Bellini et al., 2017a](#), for a comparison). A subset of stars in the wings were selected to check the spatial distribution across the image, as noise is higher in the outer regions this could have been a cause of these wings. However, the stars in the wings appear to be randomly distributed across the entire image. Although the catalogue is not cleaned, this does not pose issues for identifying the structure we expect, to be able to fit with isochrones to determine the properties. A narrow main-sequence is typical of a simple stellar population as a result of chemical homogeneity of the stars. The width of the main-sequence for NGC 5139 may be due to the unclean catalogue and noise, or this could reflect internal variations of the cluster, e.g. multiple populations. There is already a lot of supporting evidence for extensive multiple populations in NGC 5139, including from using the same data of the core shown in [Bellini et al. \(2017c\)](#). Therefore it is likely that the wide main-sequence seen is a result of this.

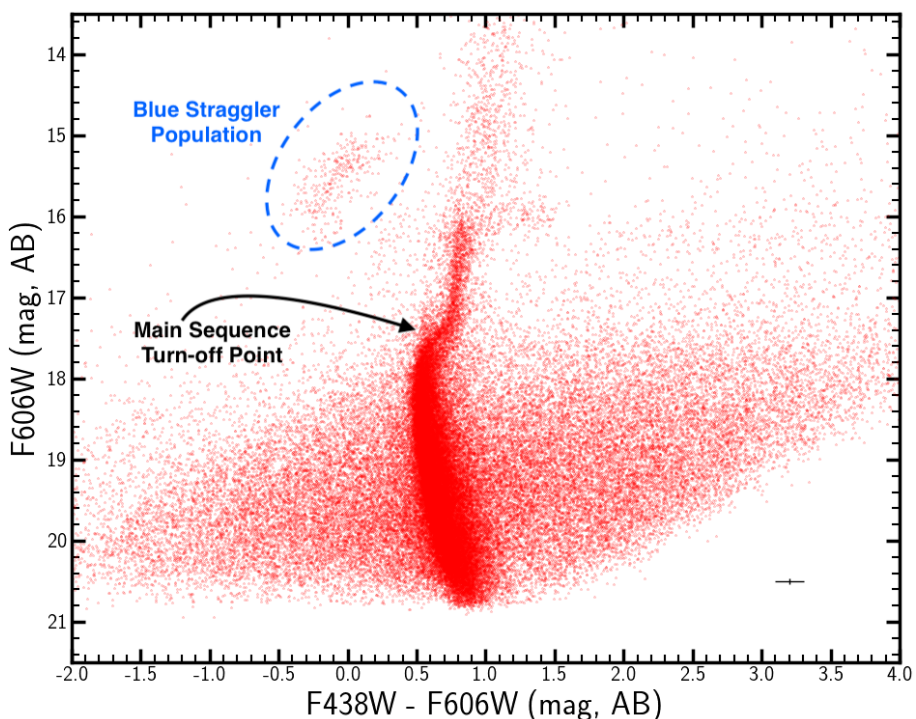


Figure 4: Colour-magnitude diagram for NGC 5139 constructed using the stellar catalogues produced in this study. The magnitudes are calculated using Mag-Auto, with typical errors in F606W magnitude of 0.04 and in F438W-F606W magnitude (calculated in quadrature) of 0.10, shown in the right bottom corner of the plot. There is a clear main-sequence turn off point leading to the red giant branch of stars. There also appears to be a blue straggler cloud, typical of Galactic globular clusters.

Another interesting aspect of Figure 4 is the blue straggler population that we seem to be able to identify. Blue stragglers are seen as an extension of the main-sequence, past the turn-off point, and have been observed to be present in all globular clusters in the Milky Way ([Piotto et al., 2004](#)). Their position in the CMD suggests that they are younger than the rest of the stars in the cluster, however, since GCs today are free of gas and dust, it is not possible for these stars to have formed by any ongoing star formation. The most popular formation mechanisms are that blue stragglers formed either via stellar collisions of two or more cluster members, or via accretion from a binary star pair ([Davies et al., 2004](#)). It is also interesting to note that when constructing the CMD with magnitudes measured with the 1 arc-second aperture, we do not see a clear blue straggler population. This is likely because blue stragglers are hotter, bluer, more massive stars than those on the main-sequence and so while we are still capturing the main-sequence star's flux with this smaller aperture, we are only capturing a fraction of the flux for these more massive

stars, and thus they appear fainter and lie in another region of the CMD. This catalogue for NGC 5139 comes from deep images of the core of the cluster. Since the cores of globular clusters are more densely populated than the outskirts, there is a high rate of stellar collisions of stars in the core, and therefore blue stragglers are most likely to be found in these regions (e.g. [Baldwin et al., 2016](#)). The fact that we find this population of stars in our data of NGC 5139 supports the idea that they may have formed by stellar collisions in the core. However, no conclusions can be drawn from this without studying the individual potential blue stragglers in more detail, which is beyond the scope of this study. While we cannot confirm that this potential blue straggler population are in-fact what we think they are, we are able to attempt to identify them in our images. Using the images in F814W, F606W and F438W of the core of NGC 5139 as the *R*, *G* and *B* respectively and correcting the astrometry slightly such that corresponding stars lined up, a colour image for this cluster was created. The subset of blue stragglers were then identified in the image, shown in Figure 5, and it can be seen that these stars are blue in colour, significantly bluer than surrounding stars. From the subset outlined in Figure 4 an estimate of 318 stars out of the total 75,88 stars in the catalogue, are possible blue stragglers.

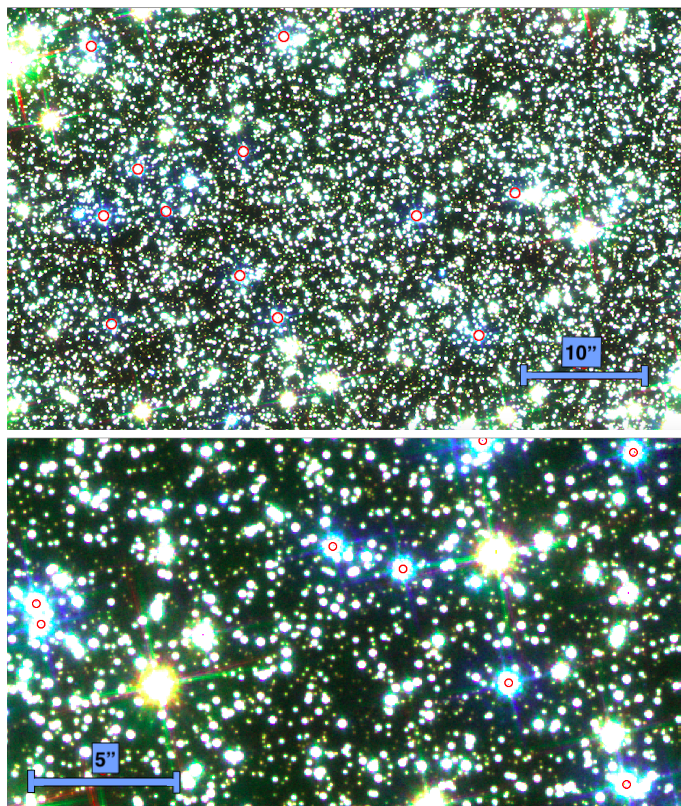


Figure 5: Sections of the RGB image of NGC 5139 using F814W, F606W and F438W images as *r*, *g* and *b* respectively. Blue straggler stars identified from the CMD for this cluster are circled in red, and are bluer in colour than the rest of the population.

3.2 Determining Cluster Properties

The next stages of the project requires the assumption to be made that the GCs in the sample can be modelled as a simple stellar population and can be represented by a single isochrone. This section outlines the stellar isochrones used, along with the method used for fitting these to the CMDs constructed from stellar catalogues, in order to measure the GCs properties.

3.2.1 Dartmouth Stellar Evolution Database

As mentioned in Section 2.2 the *Dartmouth Stellar Evolution Database* of isochrones were developed specifically to accompany a selection of the HST data that is also used in this study, making it the sensible choice of stellar evolutionary models to adopt (Dotter et al., 2008). The isochrones models are available for stellar populations of ages from 2.0 Myrs to 15.0 Gyrs and [Fe/H] from -2.5 to 0.5 dex (Dotter et al., 2008). For this study models were generated for a stellar population with ages from 8.0 to 14.0 Gyrs in steps of 0.1 Gyrs, [Fe/H] of -2.5 to 0.5 in steps of 0.5 dex and colour excesses of 0.0 to 1.0 in steps of 0.1. The colour excess, $E(B-V)$, is a measure of the dust along the line of sight, arising from light scattering off the dust in the interstellar medium (Mathis, 1990). While the models extend to lower ages, none of the globular clusters in our sample are younger than 8 Gyrs.

Since the isochrone magnitudes are intrinsic, corrections were needed to be able to compare these with observational data from the stellar catalogues, in order to be able to determine the best-fit properties for each cluster. All of the models were generated at a distance of 10 pc such that the magnitudes given are absolute and could then be converted into apparent magnitudes when matching to the catalogue data, obtaining an estimate of the distance to the cluster. This is known as main-sequence fitting (e.g. Sandage, 1970; O’Malley et al., 2017). The extinction, $E(B-V)$, was quantified in order to shift the intrinsic magnitudes into observed to match with the stellar catalogues. The commonly adopted $E(B-V)$ was chosen for this study and converted into an extinction per band using the Calzetti extinction curve for stellar populations (Calzetti et al., 1994). The extinction curve, is a function of $E(B-V)$, providing a measure of the dust as a function of wavelength (A_λ) through:

$$\frac{A(\lambda)}{E(B-V)} = a + \frac{b}{\lambda} + \frac{c}{\lambda^2} + \frac{d}{\lambda^3} \quad (3.5)$$

where a, b, c, d are constants for a given filter centred on wavelength λ . The correction from intrinsic to observed magnitudes $m_{0,\lambda}$ for each filter is thus given by,

$$A_\lambda = m_\lambda - m_{0,\lambda} \quad (3.6)$$

where m_λ is the intrinsic magnitudes given in the model and A_λ is calculated from the dust curve. Therefore through converting the theoretical isochrone model magnitudes into observed magnitudes, at a certain distance and extinction that fits to the CMD data of each globular cluster, we are able to obtain estimates for the clusters age and [Fe/H], as well as the distance to the cluster and the colour excess along the line of sight.

3.2.2 Fitting Models

In order to fit isochrones to the CMD data for each GC, the data was binned, otherwise it would be too computationally heavy to compute the fits using every star in the catalogue. Data was binned in terms of F606W intervals and the F606W - F438W colour index calculated as the median of all stars in that bin. Lower and upper errors in the colour per bin were calculated as the 16th and 84th percentiles of the distribution respectively, such that we are capturing 68% of the stars in the bin. The error bars are taken into account as weightings for the fitting. In some cases, e.g. NGC 5139, the wings of the CMD are very densely populated which skews the median colour and also the errors for each F606W mag bin. Since for fitting the models to obtain cluster properties estimates we are only interested in representing the main-sequence and turn-off point, the wings were removed from the bins by sigma clipping the data. Other structures such as the blue straggler clouds that are present in some of the CMDs were also removed from binning the data, see example Figure 6.

The properties from Harris (1996) for each GC in our sample were used to obtain an initial estimate for an isochrone that fits the data by eye. Then a wider range of isochrones around this initial

estimate were included in an attempt to fit the data more robustly. For each model, the χ^2 was calculated using,

$$\chi^2 = \sum \frac{|D - I|^2}{\sigma^2} \quad (3.7)$$

where D corresponds to the median colour of the bin, I the colour of the isochrone at that F606W mag, and σ the average error in colour. Then the reduced χ^2 was calculated using the following,

$$\bar{\chi}^2 = \frac{\chi^2}{N - d} \quad (3.8)$$

where N is the number of data points (the number of bins) and d is the number of degrees of freedom. There are four free parameters for the models: age, metallicity, distance and extinction. There is also an extra degree of freedom corresponding to the choice of model, therefore for fitting the isochrones we take d to be 5. The model with the minimum $\bar{\chi}^2$ is the best-fit and those within $\bar{\chi}_{\min}^2 + 1$ correspond to the models within 1σ of the best-fit. Estimates for the properties of the clusters are thus taken to be the median values of those corresponding to all models within 1σ , with lower and upper errors calculated as the 16th and 84th percentiles respectively.

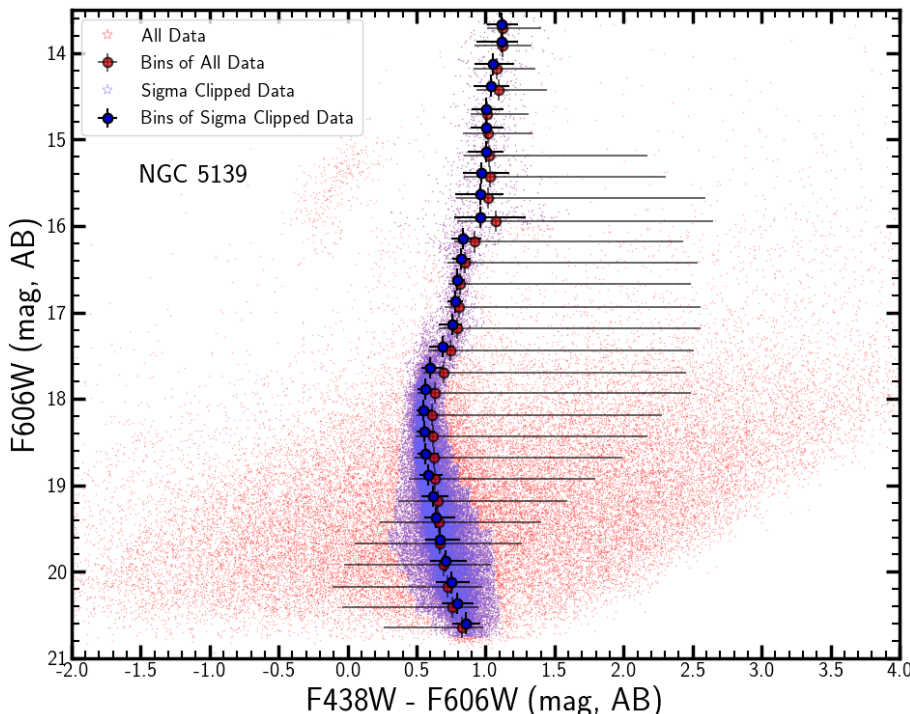


Figure 6: Colour-magnitude diagram for NGC 5139 constructed using stellar catalogues produced in this study. The data is sigma clipped using 20 iterations to represent only the main-sequence and turn off point. Red points represent the original data and corresponding bins, while blue points represent the sigma clipped data and the corresponding bins. Red bins are displaced by $+0.05$ magnitudes in the y-direction for visualisation purposes.

4 Observational Results

For each of the globular clusters in the sample a CMD was constructed from the stellar catalogues and where possible isochrones were fit to obtain an estimate of the clusters properties. Through investigating with the isochrone fitting, it was found that removing the red giant branch from the fit allowed for a better capturing of the main-sequence and turn off point structure, which gives the best estimates of the properties.

4.1 NGC 5139

The best-fit isochrones for NGC 5139, shown in Figure 7, span a range of parameters, with each giving an estimate for the cluster's age, metallicity, distance and extinction. The median of each of these parameters for the 5,342 isochrones that are within 1σ are taken to be the best-fit values, with lower and upper errors calculated as the 16th and 84th percentiles respectively. For a given distance and extinction (that of the minimum χ^2 model) the spread of the main-sequence was found to correspond to an age spread of 2.5 Gyrs or metallicity spread of 0.5 dex. The spread in metallicity appears to be greater and could be up to ~ 1 dex, in agreement with past results (Calamida et al., 2020), however, our models are limited at $[\text{Fe}/\text{H}] = -2.5$ dex. Although we cannot visually see a split of the main-sequence for NGC 5139, the spread suggests that there are multiple populations, in agreement with past literature (e.g. Bellini et al., 2017c; Calamida et al., 2020). The scatter of the data could be reduced by removing non-cluster members and by applying a differential reddening map, e.g. that of the core of NGC 5139 shown in Bellini et al. (2017b).

Property	Masked RGB Estimate	Unmasked Estimate	Literature
Age (Gyrs)	$11.5^{+2.0}_{-2.0}$	$12.0^{+1.5}_{-2.5}$	12.6 ¹
$[\text{Fe}/\text{H}]$ (dex)	$-1.9^{+0.6}_{-0.4}$	$-2.2^{+0.3}_{-0.3}$	-1.62 ²
Distance (kpc)	$5.3^{+0.7}_{-0.7}$	$5.1^{+0.9}_{-0.7}$	6.3 ²
$E(B-V)$	$0.4^{+0.1}_{-0.1}$	$0.5^{+0.1}_{-0.1}$	0.11 ³

Table 5: Properties of NGC 5139 derived from fitting isochrones to both the unmasked and RGB masked data, along with literature comparisons taken from [1] Kharchenko et al. (2016), [2] Harris (1996), [3] Peterson (1987).

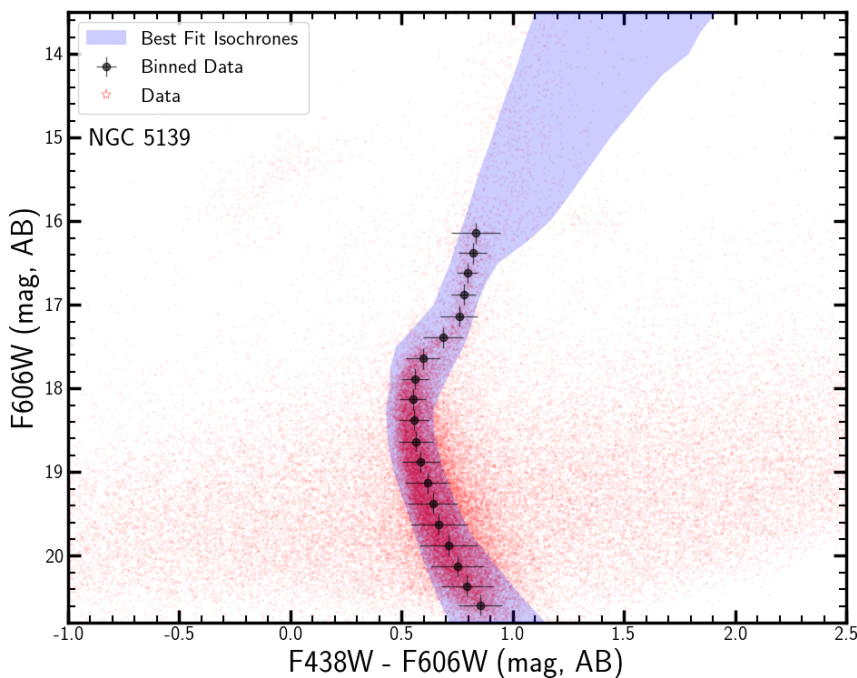


Figure 7: Colour-magnitude diagram for NGC 5139 constructed using the stellar catalogues produced in this study. Black points show the binned data used for fitting to the isochrones. The 5,342 isochrones that are within 1σ of the minimum are shown shaded in blue, the median of which is used as the best-fit estimates for cluster parameters.

4.2 NGC 3201

The best-fit isochrones for NGC 3201 are shown along with the CMD data in Figure 8 and best-fit properties derived from this in Table 6. For NGC 3201 there are 4,636 isochrones within 1σ of the minimum χ^2 . The main-sequence for this GC is much more tightly constrained, signifying that it better resembles a single stellar population than NGC 5139 does. The age and metallicity estimates are within reasonable agreement with the literature, shown in Table 6, however, the distance estimate is almost half that of literature, suggesting either a mistake in the ZP used or an outdated literature estimate from [Harris \(1996\)](#).

Property	Masked RGB Estimate	Unmasked Estimate	Literature
Age (Gyrs)	$11.0^{+2.0}_{-2.5}$	$12.5^{+0.5}_{-1.0}$	12.1^1
[Fe/H] (dex)	$-1.6^{+0.7}_{-0.6}$	$-2.1^{+0.2}_{-0.3}$	-1.48^2
Distance (kpc)	$4.5^{+0.5}_{-0.5}$	$4.2^{+0.4}_{-0.5}$	8.9^2
E(B-V)	$0.5^{+0.2}_{-0.2}$	$0.7^{+0.1}_{-0.1}$	0.21^3

Table 6: Properties of NGC 3201 derived from fitting isochrones to both the unmasked and RGB masked data, along with literature comparisons taken from [1] [Kharchenko et al. \(2016\)](#), [2] [Harris \(1996\)](#), [3] [Peterson \(1987\)](#).

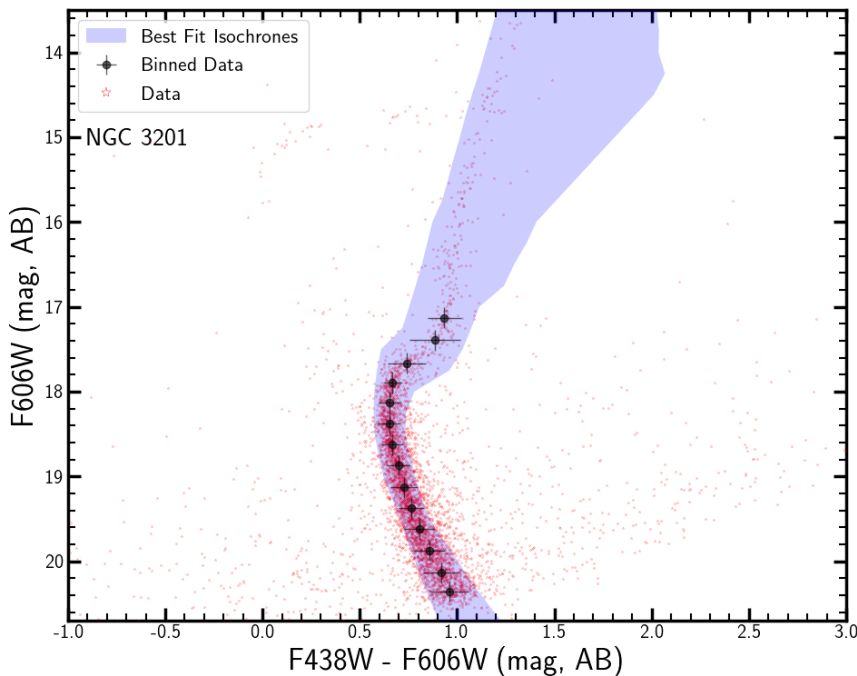


Figure 8: Colour-magnitude diagram for NGC 3201 constructed using the stellar catalogues produced in this study. Black points shows the binned data used for fitting to the isochrones. The 4,636 isochrones that are within 1σ of the minimum are shown shaded in blue, the median of which is used as the best-fit estimates for cluster parameters.

4.3 NGC 5466

Results for NGC 5466 are presented in Figure 9 and Table 7. In this case only results for fitting to the RGB masked binned data is shown as fitting to the unmasked data produced significantly larger χ^2 values such that there were only two models within $\bar{\chi}^2_{\min} + 1$, which was not sufficient enough to obtain property estimates from. This is likely due to limitations in the isochrones for modelling the RGB phase for stars. However, upon masking the RGB there are 1,117 isochrones within $\bar{\chi}^2_{\min} + 1$ shown by the blue shading in Figure 9.

Property	Masked RGB Estimate	Literature
Age (Gyrs)	$10.5^{+2.0}_{-1.5}$	12.6^1
[Fe/H] (dex)	$-1.8^{+0.3}_{-0.4}$	-2.22^2
Distance (kpc)	$15.1^{+0.6}_{-0.7}$	16.9^2
E(B-V)	$0.2^{+0.1}_{-0.1}$	0.00^3

Table 7: Properties of NGC 5466 derived from fitting isochrones to the RGB masked data and literature comparisons taken from [1] Kharchenko et al. (2016), [2] Harris (1996), [3] Peterson (1987).

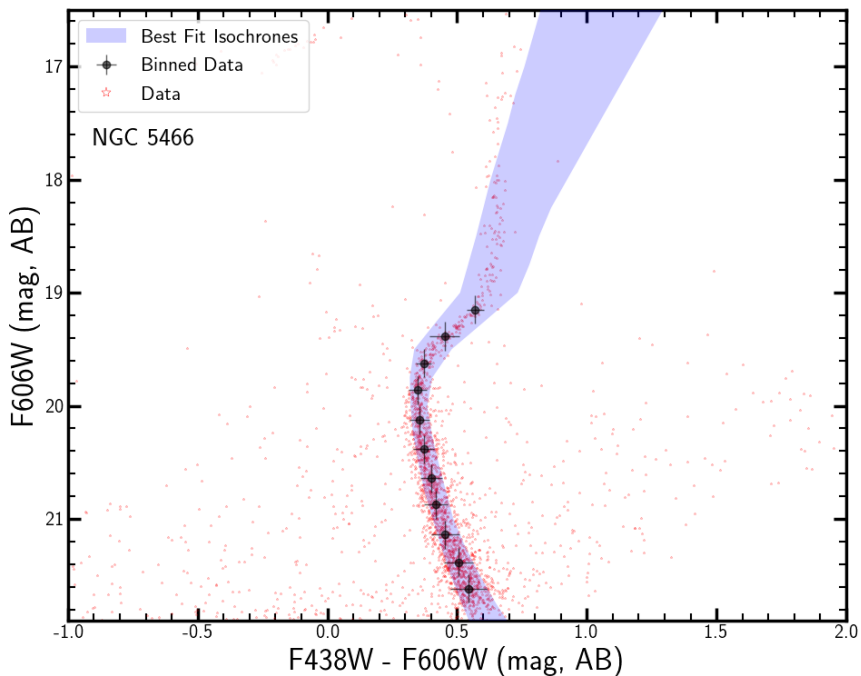


Figure 9: Colour-magnitude diagram for NGC 5466 constructed using the stellar catalogues produced in this study. Black points shows the binned data used for fitting to the isochrones. The 1,117 isochrones that have a χ^2 within 1σ of the minimum are shown shaded in blue, the median of which is used as the best-fit estimates for cluster parameters.

4.4 NGC 6934

As can be seen in Figure 10, the stellar catalogues produced for NGC 6934 have a significant amount of noise and only a very faint structure resembling a main-sequence and turn-off point, thus making binning the data difficult. Instead of sigma clipping, the data was binned using cuts in colour such that the bins visually represent the faint main-sequence and turn-off. This reduces the accuracy compared with sigma clipping, however, it was done in order to see if the properties could be determined from manually discounting the stars in the wings and focusing on this faint structure. There were 8,761 isochrones that lie within 1σ of the best-fit, shown shaded in blue in Figure 10, and the medians of the properties were then taken as the clusters estimates, shown in Table 8. The large number of best-fit isochrones is likely a reflection of visually binning the data and the low number of bins. Significantly better catalogues are needed to improve this and further constrain the properties from a more well defined main-sequence and turn-off point (see e.g. [Piotto et al., 1999](#); [Marino et al., 2018](#), for improved CMDs).

Property	Masked RGB Estimate	Literature
Age (Gyrs)	$11.0^{+2.0}_{-2.0}$	12.6^1
[Fe/H] (dex)	$-1.7^{+0.6}_{-0.6}$	-1.54^2
Distance (kpc)	$14.5^{+1.0}_{-1.2}$	12.4^2
$E(B-V)$	$0.4^{+0.1}_{-0.2}$	0.09^3

Table 8: Properties of NGC 6934 derived from fitting isochrones to both the unmasked and RGB masked data, along with literature comparisons taken from [1] [Kharchenko et al. \(2016\)](#), [2] [Harris \(1996\)](#), [3] [Kaluzny et al. \(2001\)](#).

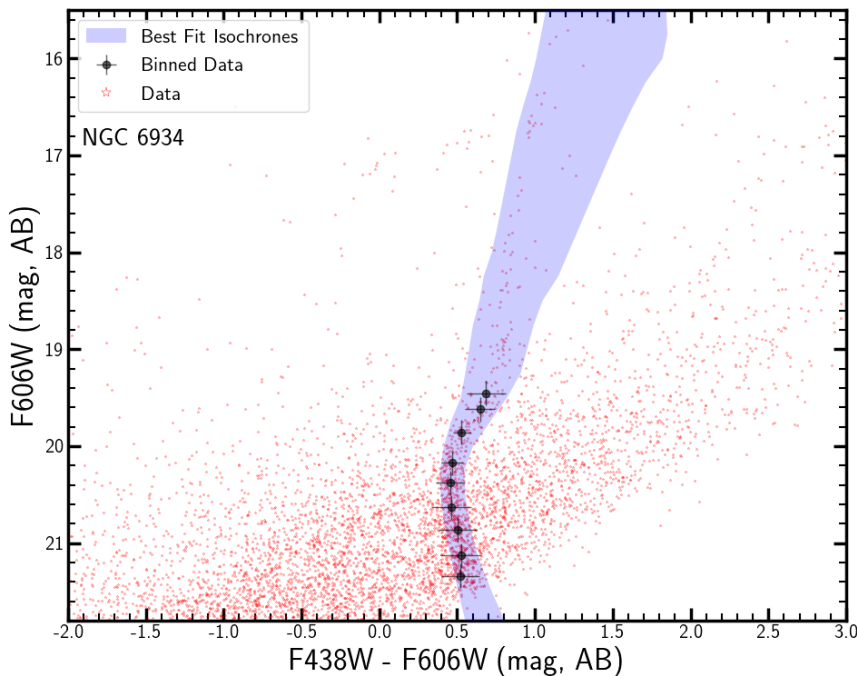


Figure 10: Colour-magnitude diagram for NGC 6934 constructed using the stellar catalogues produced in this study. Black points show the binned data used for fitting to the isochrones. The 8,761 isochrones that have a χ^2 within 1σ of the minimum are shown shaded in blue, the median of which is used as the best-fit estimates for cluster parameters.

4.5 NGC 6441 and NGC 6624

For NGC 6441 and NGC 6624 the properties were not able to be derived from fitting isochrones because the CMDs produced did not exhibit the structure required for this. Both clusters are in the direction of the Galactic bulge where extinction can be a problem for observations (e.g. see [Gonzalez et al., 2012](#), for an extinction map of the Milky Way bulge.). For these two clusters we instead use values for the ages and distances in the next stages of this study taken from literature. We adopt age estimates of 11.2 and 8.9 Gyrs ([Kharchenko et al., 2016](#)) and distance estimates of 9.7 and 7.9 kpc ([Harris, 1996](#)) for NGC 6441 and NGC 6624 respectively.

5 Generating Clusters and Turning Back the Clock

In order to produce HST images of young globular clusters, the initial mass function is needed to place stars of different masses into the image. Through making the necessary assumptions governed by stellar evolution models, we can derive this from the present-day mass function.

5.1 Present-day Mass Functions

The initial mass function (IMF) for stars can be modelled as the following,

$$\frac{dN}{dM} = AM^\alpha \quad (5.1)$$

where A is the normalisation constant specific to the population of stars, α a constant that is model dependant, N the number of stars and M the mass. This study adopts a [Salpeter \(1955\)](#) IMF such that $\alpha = -2.35$. The IMF can be used to find the total mass of stars between two mass limits M_1 and M_2 using,

$$M_{tot} = \int_{M_1}^{M_2} AM^{\alpha+1} dM \quad (5.2)$$

and so if the limits in mass span the entire range of available masses then we can estimate the total mass in a star cluster. If we assume that the initial mass function has not evolved over time, except for losing the high mass stars, we can estimate the normalisation factor from the total mass of the globular clusters today and work backwards to obtain the IMF. For the Milky Way's globular clusters we can calculate the contributions to the total mass of the different components. Assuming that the stars in a globular cluster all formed from one initial burst of star formation according to a [Salpeter \(1955\)](#) IMF, then globular clusters today will be made up of low mass stars that are still on the main-sequence and the various remnants of the more massive stars. Since the main-sequence is where a star spends $\sim 90\%$ of its lifetime, stars in the RGB phase of stellar evolution only exist here for a very short time, meaning that their contribution to the total mass can be neglected if we instead model the final stage of these higher mass stars. After the RGB phase, a star will go onto form a white dwarf (WD), a neutron star (NS) or a black hole (BH) depending on the initial mass. Therefore the total dynamical mass of globular clusters today can be assumed to consist of four components,

$$M_{tot} = M_{MS} + M_{WD} + M_{NS} + M_{BH} \quad (5.3)$$

and through the use of stellar evolutionary models, we can then calculate the normalisation factor, A , for each globular cluster. Through isochrone fitting to the CMD, an estimate for the age of each GC was obtained, shown in Section 4. The age tells us that any stars with a lifetime shorter than this will have already left the main-sequence, and those with a lifetime greater will still be on the main-sequence. Since lifetime relates directly to the mass of a star, $\tau_{MS} \propto M^{-3}$, we can estimate the main-sequence turn off mass, M_{MSTO} , that corresponds to a star with a lifetime equal to the age of the cluster. All stars below this mass will have lifetimes that are longer than the age of the

cluster and will still be on the main-sequence. The M_{MSTO} is derived from the proportionality with age using solar values for scaling as shown here,

$$\frac{\text{age}}{\tau_{\odot}} = \left(\frac{M_{\text{MSTO}}}{M_{\odot}} \right)^{-3} \quad (5.4)$$

and is used to calculate the mass in main-sequence stars, M_{MS} component, for the cluster according to,

$$M_{\text{MS}} = \int_{0.1M_{\odot}}^{M_{\text{MSTO}}} AM^{\alpha+1} dM \quad (5.5)$$

with $0.1 M_{\odot}$ corresponding to the lowest mass possible for a star to fuse hydrogen and evolve onto the main-sequence ([Straka, 1971](#)). Table 9 shows the MSTO masses derived for each GC in the sample from the age estimates obtained through isochrone fitting to the CMD. The MSTO masses (M_{MSTO}) for all of the GCs in the sample are around $1 M_{\odot}$ which is typical of globular clusters. Their old ages imply that all O, B and A type stars have already left the main-sequence. These stars will have evolved into the various different stellar remnants according to their initial mass. Through making assumptions about the final mass, we can find the other contributions to the total mass of globular clusters today. As a star evolves off the main-sequence a lot of the initial mass will be lost through stellar winds while the rest of the stars initial mass will be locked into a remnant that will remain in the cluster and contribute to the total mass. The gas produced as stars evolve is typically blown out from the cluster due to the low escape velocities, several tens km s^{-1} ([Kuranov & Postnov, 2006](#)), and any that does remain is thought to be swept from the cluster as its orbit passes through the Galactic plane ([Smith et al., 1990](#)). This means that young GCs have a higher mass than they do today.

Cluster	Age (Gyrs)	$M_{\text{MSTO}} (M_{\odot})$
NGC 5139	11.5	0.954
NGC 3201	11.0	0.969
NGC 5466	11.5	0.984
NGC 6934	11.0	0.969
NGC 6441*	11.2	0.963
NGC 6624*	8.9	1.040

Table 9: MSTO masses derived from the age estimates of all clusters in the sample that were obtained previously with the isochrones. For NGC 6441 and NGC 6624 [*], where an age could not be determined from the CMDs, literature values from [Kharchenko et al. \(2016\)](#) were used instead to derive a MSTO mass.

Firstly, stars with an initial mass less than $8 M_{\odot}$ will not go supernova but will evolve into white dwarfs that have a range of final masses ([Weidemann & Koester, 1983](#)). This distribution strongly peaks at $0.6 M_{\odot}$ and so for simplicity we can assume that all WDs will end up at this mass ([Kepler et al., 2007](#)). Therefore we can calculate the total mass of WDs in our globular clusters as

$$M_{\text{WD}} = \int_{M_{\text{MSTO}}}^{8M_{\odot}} 0.6AM^{\alpha} dM \quad (5.6)$$

where A and α are the same as previously for the MS stars.

During a supernova, a large amount of mass is lost through the strong winds that blows the gas out of the cluster. A small amount of gas is thought to have remained in the cores of globular clusters produced by the intermediate mass stars ($\sim 3 - 6 M_{\odot}$) low velocity stellar winds (lower than the escape velocity of the cluster, possibly leading to the self-pollution of lower mass stars. This is one possible explanation for chemical abundance variations seen in present-day GCs ([Ventura et al., 2001](#)).

Stars with initial masses greater than $8 M_{\odot}$ will all go supernova. Stars with masses up to $\sim 25 M_{\odot}$ ([Heger et al., 2003](#)) will likely become neutron stars, which have an average final mass of $\sim 1.4 M_{\odot}$ ([Carriere et al., 2003](#)). Therefore we can calculate the mass contribution of neutron stars in globular clusters as

$$M_{\text{NS}} = \int_{8M_{\odot}}^{25M_{\odot}} 1.4AM^{\alpha}dM \quad (5.7)$$

again with the same A and α .

Finally, stars with an initial mass greater than $25 M_{\odot}$ will become black holes after having gone supernova ([Heger et al., 2003](#)). An upper limit of $10 M_{\odot}$ ([Woo & Urry, 2002](#)) can be used to calculate the maximum mass that BHs formed this way may contribute in globular clusters. This is calculated as

$$M_{\text{BH}} = \int_{25M_{\odot}}^{120M_{\odot}} 10AM^{\alpha}dM \quad (5.8)$$

assuming all stars with masses greater than $25 M_{\odot}$ go on to form a $10 M_{\odot}$ BH. This modelling assumes that all stellar remnants produced actually remain in the cluster, which is likely the case for white dwarfs due to the low energy production. NSs and BHs, however, are produced during high energy supernova and can gain large enough velocities to escape the GC. Upon formation, both NSs and BHs undergo what is called a ‘natal kick’, a consequence of the asymmetry of supernova ejecta ([Fryer, 2004](#)), which can result in speeds greater than the escape velocity of the cluster. Therefore the number of high mass stellar remnants (NSs and BHs) in GCs today will actually be lower than in this model. While the number of BHs in globular clusters is uncertain ([Kulkarni et al., 1993](#)), the number of neutron stars is thought to account for less than 2% of the total mass. Studies suggest that although these stars account for little of the total mass of the cluster, they could have a big effect on disruption and reducing the lifetime of GCs (e.g. see [Contenta et al., 2015](#)).

Cluster	A/ 10^6	Mass (M_{\odot})				
		Total	MS	WD	NS	BH
NGC 5139	0.872	3.55×10^6	3.04×10^6	0.43×10^6	0.04×10^6	0.07×10^6
NGC 3201	0.037	1.49×10^5	1.28×10^5	0.18×10^5	0.02×10^5	0.03×10^5
NGC 5466	0.011	4.56×10^4	3.93×10^4	0.05×10^4	0.06×10^4	0.09×10^4
NGC 6934	0.029	1.17×10^5	1.01×10^5	0.13×10^5	0.01×10^5	0.02×10^5
NGC 6441	0.302	1.23×10^6	1.06×10^6	0.13×10^6	0.01×10^6	0.03×10^6
NGC 6624	0.018	7.31×10^4	6.37×10^4	0.70×10^4	0.09×10^4	0.15×10^4

Table 10: Mass of stars for the different components for each cluster with the normalisation factor used, calculated from the total masses taken from [Baumgardt & Hilker \(2018\)](#).

Cluster	A/ 10^6	Number				
		Total	MS	WD	NS	BH
NGC 5139	0.872	1.45×10^7	1.38×10^7	0.06×10^7	0.003×10^7	0.0007×10^7
NGC 3201	0.037	6.06×10^5	5.78×10^5	0.27×10^5	0.013×10^5	0.003×10^5
NGC 5466	0.011	1.85×10^5	1.77×10^5	0.08×10^5	0.004×10^5	0.001×10^5
NGC 6934	0.029	4.76×10^5	4.54×10^5	0.21×10^5	0.01×10^5	0.002×10^5
NGC 6441	0.302	5.00×10^6	4.77×10^6	0.22×10^6	0.01×10^6	0.003×10^6
NGC 6624	0.018	2.95×10^5	2.83×10^5	0.12×10^5	0.006×10^5	0.002×10^5

Table 11: Number of stars for the different components for each cluster with the normalisation factor used.

Using the total mass of each globular cluster from the literature, the normalisation for the mass function (A) can be calculated and then used to calculate the mass of each component. The total

dynamical mass of each of the globular clusters in the sample is taken from [Baumgardt & Hilker \(2018\)](#) which were determined by fitting a large set of N-body simulations to the velocity dispersions and surface brightness profiles. The total mass, as well as the individual mass and number contributions of each of the different components, for each cluster, are shown in Tables 10 and 11.

As can be seen in Table 10 most of the mass in a cluster resides in the main-sequence stars, a significant amount in the white dwarfs and only negligible amounts in the neutron star and black hole components. For example, looking at NGC 5139 the main-sequence stars make up 85.7% of the total mass of the cluster, white dwarfs make up 11.0%, neutron stars only 1.2% and black holes 2.1%. This is a maximum mass of the neutron star and black hole components, assuming that no neutron stars and black holes are lost from the cluster over its lifetime which, as discussed previously, studies suggest not to be the case. Since the black holes and neutron stars only contribute a small fraction of the total mass of the globular clusters they can be discounted from calculating the normalisation factor A . However, the white dwarfs contribute a significant amount of mass to the cluster such that they cannot be ignored for calculating the normalisation. The assumption that the white dwarfs have a final mass of $0.6 M_{\odot}$ is an established one, whereas the assumptions and approximations for the neutron stars and black holes are not as robust. When A is calculated only accounting for main-sequence stars and white dwarfs as the total mass of the cluster today, the MS stars contribute 88.7% of the mass and the WDs 11.3% for NGC 5139, which is not significantly different to that found when taking into account neutron stars and black holes. Therefore, for modelling the GCs mass function today, we take the dynamical mass of each cluster from [Baumgardt & Hilker \(2018\)](#) to be equal to the mass of the main-sequence stars up to the turn-off point and the mass of white dwarf remnants. We then solve for the normalisation factor A for each globular cluster, shown in Table 12.

5.2 Initial Mass Functions

Cluster	A	$M_{\text{tot}} (M_{\odot})$	N_{tot}
NGC 5139	9.01×10^5	5.28×10^6	14.9×10^6
NGC 3201	0.38×10^5	0.22×10^6	0.63×10^6
NGC 5466	0.12×10^5	0.07×10^6	0.19×10^6
NGC 6934	0.30×10^5	0.17×10^6	0.49×10^6
NGC 6441	3.12×10^5	1.83×10^6	5.17×10^6
NGC 6624	0.18×10^5	0.11×10^6	0.31×10^6

Table 12: Normalisation factor, A , used for the IMF for each cluster along with the calculated total mass and number of stars in the young clusters, assuming all stars (from 0.1 to $120 M_{\odot}$) are still on the main-sequence. The mass for each is found to be ~ 1.5 of the clusters mass today according to [Baumgardt & Hilker \(2018\)](#).

The IMF for each cluster could now be modelled using equation 5.1 with $\alpha = -2.35$ following a [Salpeter \(1955\)](#) IMF model and using the normalisation factor, A , calculated for each GC in the sample from the present-day mass functions. Assuming that the IMF has not evolved over time, we make the assumption that it still has the same form, described by equation 5.1, for young globular clusters at formation. Studies have found that the mass function of globular clusters will have changed over the clusters lifetime, e.g. [Richer et al. \(1991\)](#), however, modelling this is extremely complicated due to effects of mass segregation, loss of stars through disruption mechanisms and stellar evolution processes. In this study, we adopt the simplistic approach that the slope has remained the same and attempt to account for stellar evolution of main-sequence stars, assuming a single burst of star formation. The caveats of this are discussed further in Section 7. This assumes that A remains the same and $\alpha = -2.35$. Therefore we can obtain our IMF by assuming that all the stars have formed and are still on the main-sequence. This requires an upper and lower limit for the

masses of stars that form on the main-sequence. We adopted a lower limit for main-sequence stars of $0.1 M_{\odot}$ corresponding to the electron degeneracy limit for a star to be able to fuse hydrogen ([Straka, 1971](#)). For the upper mass limit of main-sequence stars we refer to [Oey & Clarke \(2005\)](#) that adopt an upper mass limit of main-sequence stars to be $120 - 200 M_{\odot}$ with a [Salpeter \(1955\)](#) IMF. In this study, we take our upper mass limit to be $120 M_{\odot}$, as beyond this mass the number of stars in the cluster in our model is so small that they can be considered negligible, because the IMF is a strongly declining function of mass. The IMF tells us that when star clusters form, there will be a much larger proportion of lower mass stars than high mass stars forming. The fraction of low to high mass stars for each GC in the sample will be the same, but the total number of stars of each mass range will vary according to the normalisation A .

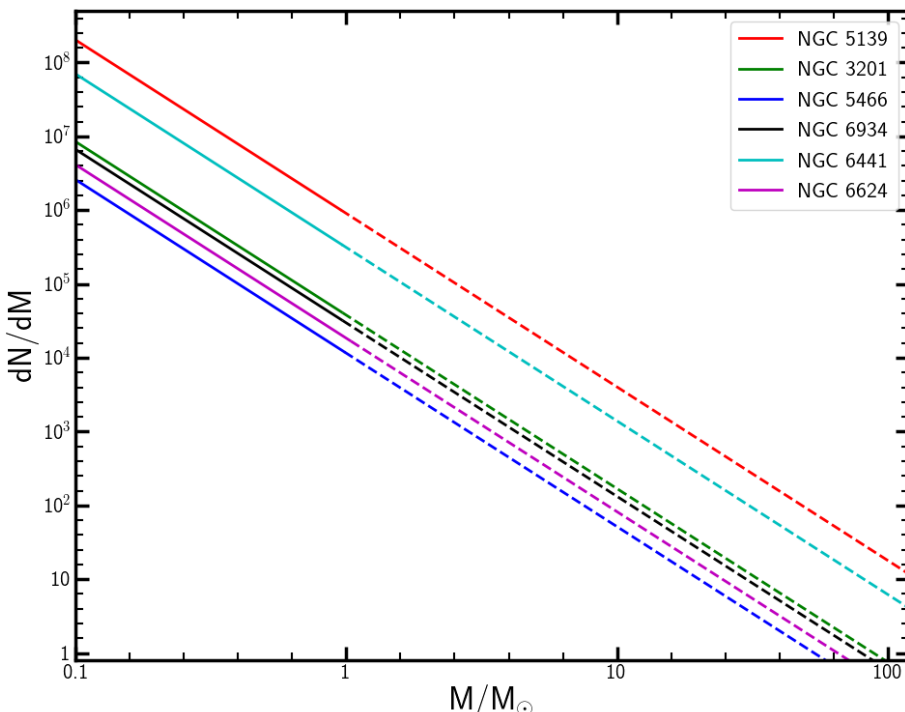


Figure 11: Initial mass functions for each globular cluster in the sample using the normalisation factor A derived using the total mass from [Baumgardt & Hilker \(2018\)](#) assuming that the total mass is equal to the mass of stars still on the main-sequence and the mass of white dwarf remnants in the cluster. For all clusters we assume a [Salpeter \(1955\)](#) IMF with $\alpha = -2.35$.

The derived IMF, shown in Figure 11, is then used for generating the young clusters and choosing the masses of the stars across the cluster. Shown in Table 12 is the total mass of each generated young globular cluster with an assumed [Salpeter \(1955\)](#) IMF of stars, with stars of all masses still on the main-sequence. In this model, the mass for each young GC is found to be ~ 1.5 of the mass estimates of the GC today from [Baumgardt & Hilker \(2018\)](#).

5.3 Mass-Temperature Relation

The stars in a cluster can be split into different spectral types according to their properties, such as temperature and mass. A star is generated according to the IMF such that it has a higher probability of being a lower mass star. The luminosity of the star is then calculated using the relation that luminosity is proportional to mass for main-sequence stars (e.g. [Smith, 1983](#)), $L \propto M^4$, and using solar values for scaling such that,

$$L = L_{\odot} \left(\frac{M}{M_{\odot}} \right)^4 \quad (5.9)$$

for any value of M. In reality this proportionality does not hold for the low and high mass limits of main-sequence stars and the power of 4 should change for different mass regimes (e.g. see [Eker et al., 2015](#), who split the masses into four regimes with four different powers of M). However, for this study, we adopt a simplistic approach which could be improved upon in the future. For a star with a given mass, and hence luminosity, we use the Stefan Boltzmann Law,

$$L = 4\pi\sigma R^2 T^4 \quad (5.10)$$

to constrain the radius and temperature of each star. The approach taken in this study is to set the temperature range for a star of a given mass and pick a temperature at random from this constrained range in order to have some variety in stars like seen in reality. Then the radius can be calculated from equation 5.10. Initially, the temperature ranges highlighted in Table 13 were used to choose a temperature given the mass of the star and therefore the spectral type ([Habets & Heintze, 1981](#)). However, this produced stars that were un-physical and instead, the mass and temperature needed to be controlled further, as the two are more intimately linked. A higher mass O type star will have a higher temperature and larger radius than a lower mass star that is also an O type.

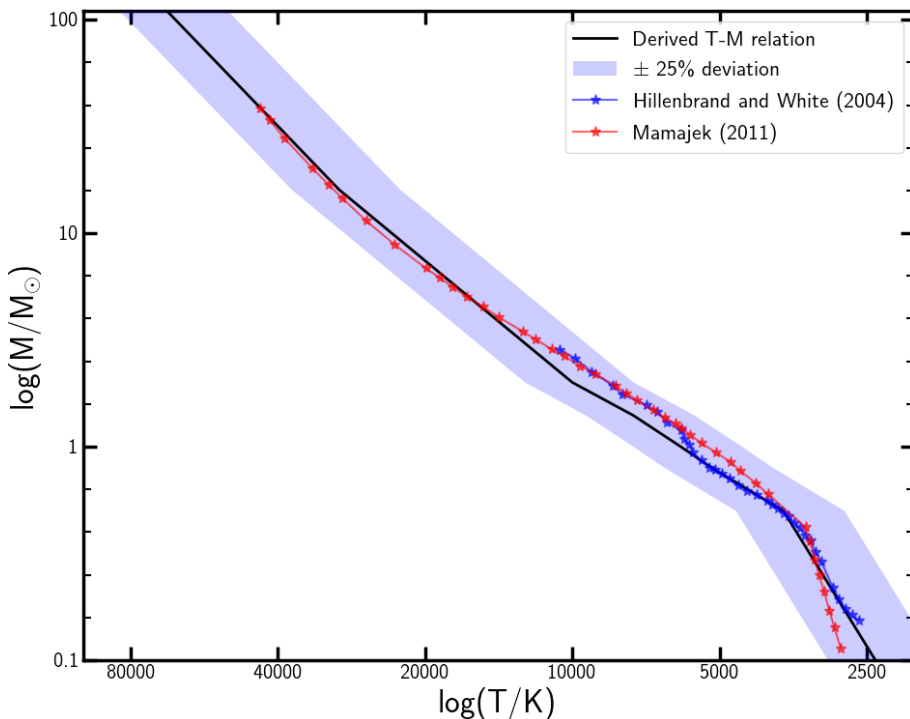


Figure 12: The temperature-mass relationship derived for stars across all masses using the lower limits of T and M from Table 13 for the initial T-M relationship (black line) and then allowing the temperature to vary by 25% as shown by the blue shading to produce variety in the stars formed. Data from two other studies, [Hillenbrand & White \(2004\)](#) and [Mamajek \(2011\)](#), are overlaid to show that they agree with this approach.

Using the lower limits of mass and temperature for the different spectral types, a T-M relation was derived, shown in Figure 12. For a star of a given mass, a temperature can be found using the relationship shown by the black line, but then the temperature is allowed to take any value within the range $\pm 25\%$ of the initial specified temperature, which is shown by the blue shading. This will produce stars of a range of temperatures that reflects the real life formation of stars, and the amount by which this can vary is chosen to encompass previous studies T-M relationships (e.g.

([Hillenbrand & White, 2004](#); [Mamajek, 2011](#)) and appear to represent the spread of main-sequence stars typically seen on a Hertzsprung-Russel diagram.

Spectral Type	Temperature Range (K)	Mass Range (M_{\odot})	Radius Range (R_{\odot})
O	30000 - 70000	16.0 - 120.0	9.5 - 100.0
B	10000 - 30000	2.0 - 16.0	1.3 - 9.5
A	7500 - 10000	1.4 - 2.0	1.1 - 1.3
F	6000 - 7500	1.0 - 1.4	0.9 - 1.1
G	5200 - 6000	0.8 - 1.0	0.8 - 0.9
K	3700 - 5200	0.5 - 0.8	0.6 - 0.8
M	2400 - 3700	0.1 - 0.5	0.1 - 0.6

Table 13: Temperature and mass ranges for each spectral type taken from Table 8 in [Habets & Heintze \(1981\)](#) and radius ranges calculated using the mass limit converted to a luminosity, the temperature limits and equation 5.10.

5.4 Black-body and Fluxes

In this work, the stars have been modelled as black-bodies such that their spectrum can be described by the Planck equation. In reality, it would be more realistic to download spectra for stars of different spectral types and temperatures using the metallicity of the cluster obtained with the isochrones, assuming all stars formed out of one gas cloud with the same metallicity. However, this proves too time consuming for this study, and so a more simplistic approach of black-bodies spectra has been chosen. The main difference between a black-body and a true spectrum is the absorption lines due to metals, and since globular clusters formed in the early Universe when there were few metals present, and are thus low in metallicity, the black-body approximation is reasonable for these stars. Previous studies (e.g. [Suzuki & Fukugita, 2018](#)) have shown that the black-body approach is reasonable for metal-poor stars.

The Planck equation describes the spectrum of a star of a given temperature and is defined as either B_{λ} or B_{ν} depending on whether it is calculated in wavelength or frequency units. In wavelength units we have,

$$B_{\lambda} = \frac{2hc^2}{\lambda^5} \frac{1}{\exp(hc/\lambda K_B T) - 1} \quad (5.11)$$

where h is Planck's constant in units of $\text{m}^2 \text{kg s}^{-1}$, K_B the Boltzmann constant in units of $\text{m}^2 \text{kg s}^{-2} \text{K}^{-1}$ and c the speed of light in units of m s^{-2} . This gives us B_{λ} in units of $\text{m}^{-1} \text{kg s}^{-3}$ which is equivalent to W m^{-3} . In order to be able to measure the AB magnitudes of the stars B_{λ} is converted into flux with standard units of $\text{erg s}^{-1} \text{cm}^{-2} \text{\AA}^{-1}$. This is done by $B_{\lambda} (\text{erg s}^{-1} \text{cm}^{-2} \text{\AA}^{-1}) = 10^{-7} B_{\lambda} (\text{W m}^{-3})$ using that $1\text{W} = 10^7 \text{erg s}^{-1}$.

B_{λ} is the spectral radiance from the surface of the star and we follow the literature (e.g. [Suzuki & Fukugita, 2018](#)) in order to convert to a flux from a certain distance, D , as follows,

$$f_{\lambda} = \pi B_{\lambda} \left(\frac{R}{D} \right)^2 \quad (5.12)$$

where R is the radius of the star.

To obtain the stars magnitude the flux needed to first be converted into frequency units, f_{ν} , due to how the AB magnitude system is defined. This can be done for the entire black-body spectrum using,

$$f_{\nu} = \frac{\lambda^2}{c} f_{\lambda} \quad (5.13)$$

with one λ in units of m to cancel out with that in c (m s^{-1}) and the other in units of \AA to cancel out with that in f_λ , giving f_ν in units of $\text{erg s}^{-1} \text{cm}^{-2} \text{Hz}^{-1}$.

Then the AB magnitude of a star in a given filter F is given by,

$$m_{\text{AB}}(F) = -2.5 \log \left(\frac{\int f_\nu R_F d\nu / \nu}{\int R_F d\nu / \nu} \right) - 48.60 \quad (5.14)$$

where R_F corresponds to the filter profile for that given magnitude, e.g. R_{F438W} will give $m_{\text{AB}}(\text{F438W})$.

The flux conversions and magnitude calculations were checked with the solar spectrum from [Mef-tah et al. \(2018\)](#) confirming the apparent and absolute magnitudes for the Sun in HST WFC3 F438W and F606W ([Willmer, 2018](#)).

5.4.1 Filter Profiles

Figure 13 shows the HST filter transmission profiles for the WFC3 and ACS filters necessary to this study. All of the original image data used in this study has been taken with HST WFC3 and ACS filters that are shown in Figure 13, so these filters are especially useful for reproducing the original data when generating the globular clusters and for producing HST images of how these clusters will have looked when they were younger. In addition to this three extra filters have been used when calculating the fluxes of the young GCs placed at high redshift, these are shown in Figure 17 and discussed further in Section 5.6. All of these filter profiles have been taken from [Rodrigo et al. \(2012\)](#); [Rodrigo & Solano \(2013\)](#).

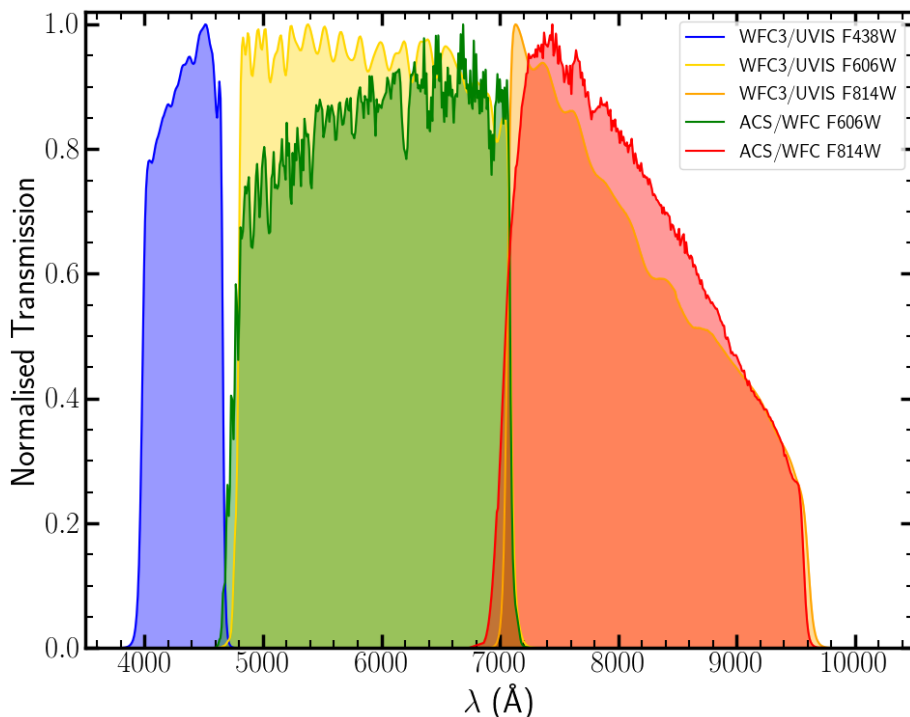


Figure 13: Normalised filter profiles and transmission for the WFC3 UVIS channel F438W, F606W and F814W filters, along with the ACS WFC channel F606W and F814W filters. These are the filters used for the image data in this study, see Section 2.2, and have been used for generating our own globular clusters. Filter profiles are taken from [Rodrigo et al. \(2012\)](#); [Rodrigo & Solano \(2013\)](#).

5.5 Positions of Stars

Another important aspect of generating globular clusters is the placing of stars in the image, as the stars will not be randomly distributed. In order to do this, each globular cluster has been modelled as a spherical system with the distribution of stars following a Gaussian distribution. This way more stars will belong in the central regions of the cluster and the number of stars will trail off towards the outskirts. The size of each globular cluster is needed in order to model this distribution and in this study we use the half-mass radius, R_h , from [Harris \(1996\)](#). This gives the size of half of the globular cluster's mass, so we can assume that half of the stars are contained within this radius, assuming that stars of all masses are distributed randomly across the cluster. This assumption is not technically correct, due to a process called mass segregation in which the high mass stars sink towards the centre of a cluster and low mass stars orbit out at greater speeds at larger radii (see e.g. [Baumgardt et al., 2008](#)). However, modelling mass segregation processes in GCs is a complex problem and beyond the scope of this report and so our assumption is reasonable. For a Gaussian distribution 50% of the data is contained within $\pm \frac{\sigma}{\sqrt{2}}$ so we can use that

$$\sigma = R_h \sqrt{2} \quad (5.15)$$

with R_h converted into units of pixels with the pixel scale, to get a Gaussian probability distribution for each stars x and y position in an image as:

$$P = \frac{\exp(-\frac{(x-x_0)^2}{2\sigma^2})}{\sum_{x=1}^{2x_0} \exp(-\frac{(x-x_0)^2}{2\sigma^2})} \quad (5.16)$$

where x_0 is the centre of the image, centred on the cluster centre.

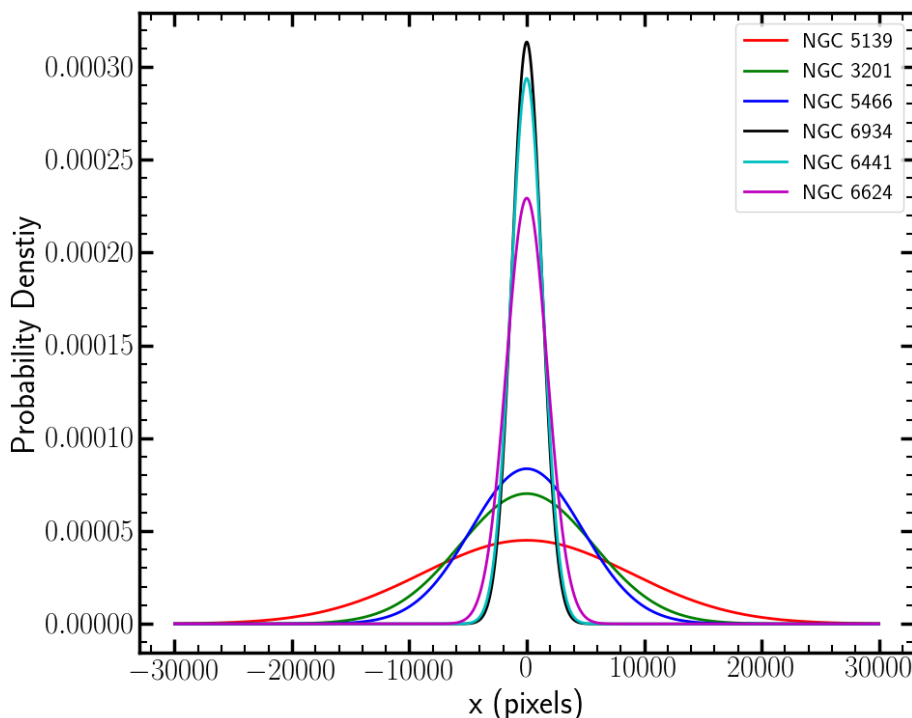


Figure 14: Normalised probability density function for each GC in the sample modelled as a Gaussian (equation 5.16) with centre $x_0 = 0$ and $\sigma = R_h \sqrt{2}$. R_h values are from [Harris \(1996\)](#), converted into units of pixels using the HST WFC3/UVIS pixel scale. The function is normalised such that the probabilities over all x sum to 1. The same is done for the y position of each star assuming spherical symmetry.

5.5.1 Number of Stars

From the initial mass functions the total number of stars in the cluster can be found via

$$N_{\text{tot}} = \int_{0.1}^{120} AM^{\alpha} dM \quad (5.17)$$

with the limits of the integration spanning the entire range of masses of stars on the main-sequence. These are shown in Table 12 for each GC in the sample. This can be used to know the number of stars to generate in each image of each globular cluster, based on the fraction of the cluster that will be included in the image. Figure 15 shows the number density for each cluster spatially. This is found by multiplying the normalised probability distribution shown in Figure 14 by the total number of stars in the cluster (shown in Table 12), such that summing the number density over all x will give the total number of stars in the cluster, N_{tot} . Therefore integrating the number density over a specified range of b pixels will give the number of stars that will be captured in an image of size $b \times b$ pixels. The images generated in this study are HST images using the WFC3/UVIS properties or ACS/WFC depending on the cluster and filter, referring to Table 2. Both WFC3/UVIS and ACS/WFC detectors are 4000 x 4000 pixels, and so we can calculate the number of stars that will be included in this region for generating our HST images.

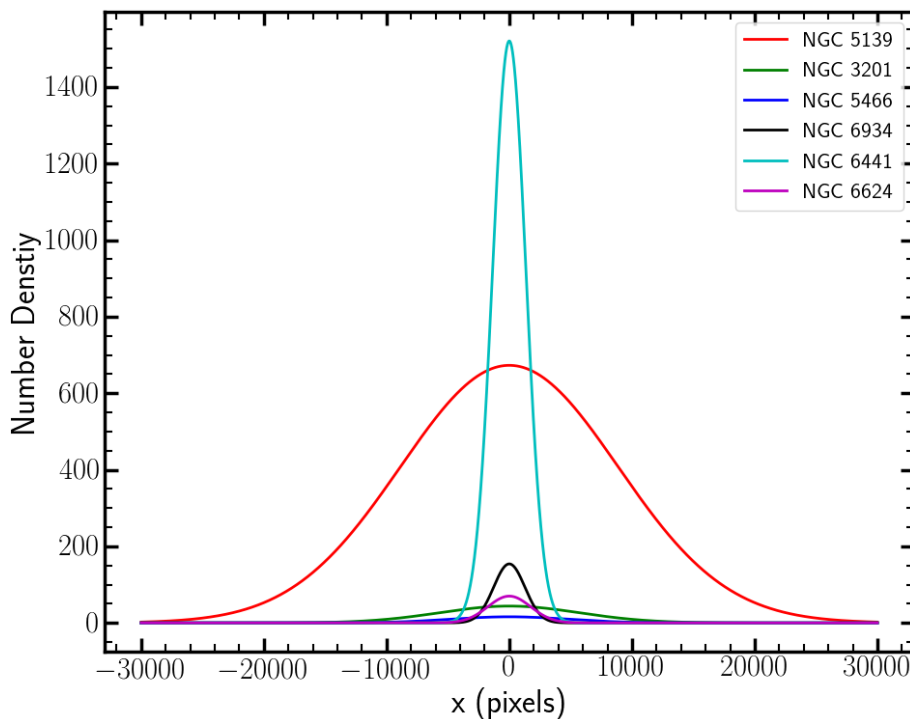


Figure 15: Number of stars as a function of x position for each globular cluster as derived from the total number of stars in the cluster, N_{tot} , and the spatial probability distribution function in Figure 14.

5.5.2 Magnitude Limit

Since there are observing limits that affect low mass stars predominantly, it is necessary to populate the generated globular clusters with only stars above the limiting magnitude. For generating the young GCs at the distance they are at in the Milky Way the magnitude limit can be taken from the stellar catalogues from the original HST data of the GCs today. For example for NGC 5139 and NGC 3201, see Figures 7 and 8, the limiting F606W magnitude appears to be ~ 21 , whereas for NGC 5466 and NGC 6934, see Figures 9 and 10, the limiting F606W magnitude appears to

be ~ 22 . This difference is likely due to the different exposure times of the data for each cluster and small variations in distances. Therefore in this study, a F606W magnitude limit of 22 has been chosen for all six Milky Way globular clusters when generating stars. This magnitude limit corresponds to a mass limit, as lower mass stars have a lower temperature and flux and therefore magnitude. We convert our F606W magnitude limit into a mass limit for stars in the generated cluster by looking at the distribution of F606W magnitudes with stars of all available masses (0.1 - $120 M_{\odot}$). For each mass (in steps of 0.1) there is a variation in F606W magnitude due to the variation in temperature allowed, shown in Figure 12. Therefore the mass limit chosen is the point at which all stars of a given mass are above the magnitude limit and therefore visible in the images generated of that cluster. It can be seen in Figure 16 that a mass limit of $1 M_{\odot}$ corresponds to the minimum mass at which all stars are above the limiting magnitude. Thus clusters can be produced by generating stars from $1 M_{\odot}$ to $120 M_{\odot}$. Cutting the low mass stars that will not be detected not only allows for a real reflection of observational data but also improves computing times due to the large number of stars that have a mass between 0.1 and $1.0 M_{\odot}$ that would otherwise need to be generated.

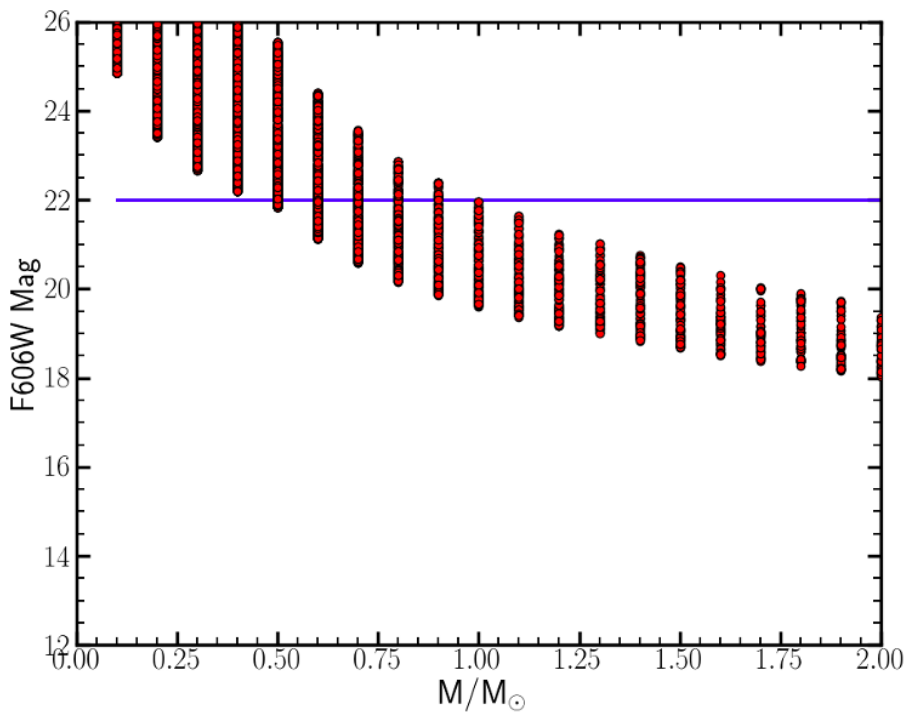


Figure 16: Stars generated for NGC 5466 with mass distribution according to the IMF and F606W magnitudes calculated for each star. The blue line shows the limiting magnitude cut of 22. Only stars below this line (lower magnitude = higher flux) will be able to be seen in the generated images. Therefore a mass limit of $1 M_{\odot}$ is taken such that for this mass and above then all stars generated are brighter than the limiting magnitude of ~ 22 .

5.6 Placing at High Redshift

As well as generating images of the young globular clusters as they appear at the distance they are at today in the Milky Way, the other aim of this study was to place these young globular clusters at high redshift and see if they could be detected with HST. This gives us an idea of how forming globular clusters will look if imaged with HST and allows a comparison between the progenitor GCs observed at high redshift (e.g. [Vanzella et al., 2017](#); [Bouwens et al., 2017](#); [Kikuchi et al., 2019](#)) to young Milky Way globular clusters placed at high redshift. In this study, we have chosen

to place the clusters at $z = 2.0$ and $z = 6.6$, corresponding to the age of the Universe when the Milky Way GCs formed (plus a couple of Myrs to allow for formation) using the lower and upper limits on the ages derived for the GCs respectively. A redshift of 6.6 also corresponds to the redshift of Lyman-alpha emitting galaxy CR7, allowing us to, in the future, place our young GCs into images of this high redshift galaxy to see if we can still identify them (see [Sobral et al., 2019](#)).

To place at high redshift, the scaling is important as cosmology comes into play. Using the angular half-mass radius of the cluster in arc-seconds from [Harris \(1996\)](#), the true size of the clusters half-mass radius can be calculated using simple geometry and the definition of a parsec. With the distance to the cluster in the Milky Way in parsecs and the angular size in arc-seconds, then the size in astronomical units (AU) can be calculated as,

$$R_h(AU) = R_h(\text{''}) D \quad (5.18)$$

where D is the distance to the cluster in the Milky Way, taken from the isochrone fitting results in Section 4. The half-mass radius can then be converted into parsecs using the scaling that $1\text{AU} = 4.85 \times 10^{-6}$ pc. This can then be used for calculating the angular size of the cluster when at high redshifts of 2.0 and 6.6. With the half-mass radius of the cluster in parsecs, the angular size of the half-mass radius in arc-seconds for at high redshift can be calculated as

$$R_h(\text{''}, D_L) = \frac{R_h(\text{pc})}{a(z)} \quad (5.19)$$

where $a(z)$ is the scale factor and D_L the luminosity distance that can be calculated for a specific redshift. The luminosity distance is used for scaling the fluxes of the stars according to equation 5.12. For $z = 2.0$ and $z = 6.6$ the scale (8.37 kpc per '' and 5.40 kpc per '') and luminosity distance (15537 Mpc and 64458 Mpc) were calculated using cosmology calculator ([Wright, 2006](#)) assuming a Λ CDM cosmology with $H_0 = 70 \text{ km s}^{-1} \text{ Mpc}^{-1}$, $\Omega_M = 0.3$ and $\Omega_\Lambda = 0.7$. The sizes of each GC in the sample in the Milky Way, at $z = 2.0$ and $z = 6.6$ are calculated, shown in Table 14.

Cluster	Milky Way		$R_h(\text{pc})$	High Redshift	
	$R_h(\text{'})$	$D (\text{pc})$		$z = 2.0$ $R_h(\text{''})$	$z = 6.6$ $R_h(\text{''})$
NGC 5139	4.18	5300	6.44	0.0008	0.0012
NGC 3201	2.68	4500	3.51	0.0004	0.0007
NGC 5466	2.25	15100	9.88	0.0012	0.0018
NGC 6934	0.60	14500	2.53	0.0003	0.0005
NGC 6441*	0.64	9700	1.81	0.0002	0.0003
NGC 6624*	0.82	7900	1.88	0.0002	0.0003

Table 14: Half-mass radius in parsecs of each GC in the sample are calculated using the angular half-mass radius from [Harris \(1996\)](#) and the distances derived using the isochrone fitting in Section 4. For NGC 6441 and NGC 6624 [*] where isochrones could not be fit to the data, distances are taken from literature estimates given by ([Harris, 1996](#)). The angular size of the half-mass radius of each cluster at redshifts 2.0 and 6.6 are calculated in arc-seconds using the scalings of 8.37 and 5.40 kpc/'' respectively ([Wright, 2006](#)).

The clusters at high redshift have been generated as they would appear if imaged with HST. The deepest observations to date is that of the Hubble Ultra Deep Field (HUDF) which is able to observe down to at least the $\sim 29^{\text{th}}$ magnitude ([Beckwith et al., 2006](#)). Assuming that it was possible to observe these high redshift young globular clusters with the same long exposure times, like that of the HUDF, there will be a limiting (AB) magnitude of ~ 29 ([Beckwith et al., 2006](#)). No single star at these high redshifts will be able to be resolved, nor will any be bright enough to have a magnitude brighter than ~ 29 . However, Table 14 shows that the angular sizes of the clusters at $z = 2.0$ and $z = 6.6$ are below the point spread function (PSF) measured for HST, from

the original WFC3 and ACS images, of $0.1''$. Therefore GCs at high redshift will be extremely compact sources that can be modelled by a single PSF. These sizes have been calculated assuming that the size of the half-mass radius in parsecs derived for the GCs in the Milky Way today, would be the same for the young GCs at high redshift. This is not strictly true as the young clusters at high redshift are more populated, more massive and therefore likely more extended in size (e.g. Phipps et al., 2019). However, since the sizes at these redshifts are many orders of magnitude smaller than the PSF for HST, of $0.1''$, this assumption is deemed valid as the clusters generated will then be set to the size of the PSF.

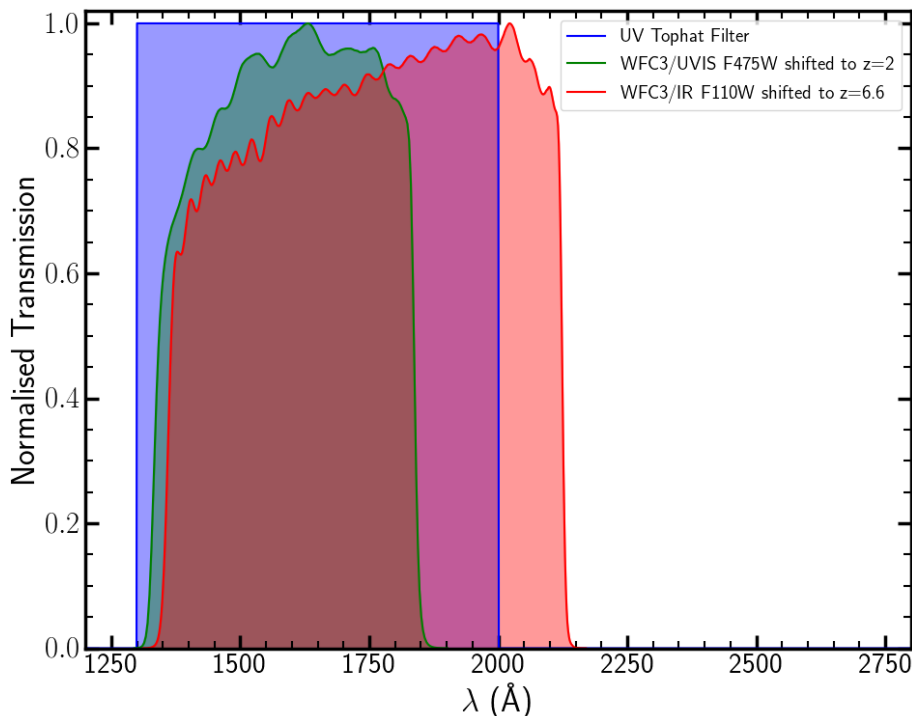


Figure 17: Normalised filter profiles and transmission for F475W and F110W that have been chosen for capturing the rest-frame UV at redshifts of 2.0 and 6.6 respectively. The filters are shown shifted to the rest-frame for the respective redshifts, as well as a top-hat perfect filter that covers the entire UV rest-frame. F475W and F110W filter profiles are taken from Rodrigo et al. (2012); Rodrigo & Solano (2013).

For generating the clusters, the flux is then summed across the total number of stars in the cluster using the IMF to produce stars across the entire mass range, like done previously. However, now at high redshift we are modelling the clusters as a single point source, a combination of stacked stars. Therefore, a magnitude of the entire cluster can be measured and the cluster can be observed only if this is below (brighter than) ~ 29 . As well as measuring the fluxes in the rest-frame F438W, F606W and F814W, the flux will also be calculated in a UV filter with large enough width to capture where the most massive stars BB spectrum will peak. While the high mass stars are rare in the clusters due to the IMF, they produce a much higher flux, which will dominate in the UV, where low mass stars produce almost no flux but high mass stars peak. If the young GCs can be observed at high redshift in any filter, it will likely be UV. Pre-existing HST filter profiles such as F475W and F110W were used that shift into the rest-frame UV for $z = 2.0$ and $z = 6.6$ respectively, using $\lambda_{\text{rest}} = \lambda_{\text{observed}} / (1 + z)$. However, these filters were not wide enough to capture the entire rest-frame UV part of the stars spectrum, and so a top-hat filter was also used to give an estimate of the UV magnitudes in the ideal case of a perfect filter spanning the whole range of UV wavelengths. The filter profiles can be seen in Figure 17 and magnitudes obtained with these are presented in Section 6.

5.7 Steps for Producing the Generated Images

Throughout Section 5 the models required for generating the HST images of young globular clusters have been presented. Shown in Figure 18 are the steps taken to use these models and produce the images that are presented in Section 6. The distance that the black-body spectrum of each star is placed at, to derive fluxes, is either that determined from isochrone fitting (Section 4) for generating the young clusters at the distance they are at in the Milky Way, or using the luminosity distance, calculated for $z = 2.0$ or $z = 6.6$, when placing at high redshift. For generating the images at high redshift, each star is generated in the same way up to step 4, as shown in Figure 18, but then the flux is summed for all stars up to the total number of stars in the cluster and only one source is placed in the image. This generates the cluster as a single point source, setting the size of the cluster to the HST PSF, for reasons outlined in Section 5.6.

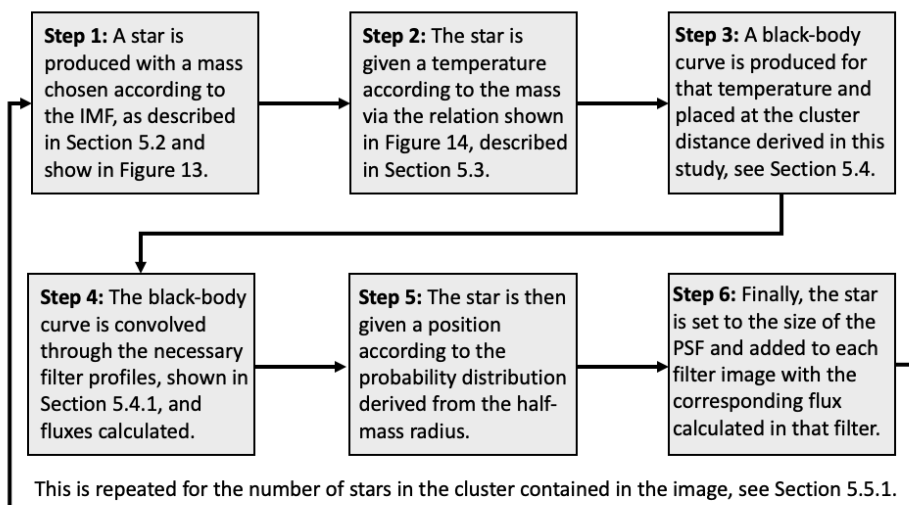


Figure 18: Steps taken to combine all of the models adopted in this study in order to generate HST images of young Milky Way globular clusters. Each image is generated by repeating the process for each star up until the number of stars in the image. The stars are all set to the point spread function (PSF) measured from the original HST images of $0.1''$.

6 Generated Results

All six of the Milky Way globular clusters included in the original sample have been modelled as they would appear when they were younger by repopulating the mass function with high mass stars. These young GCs have been generated and HST images created for the clusters at the distance they are at today in the Milky Way and at high redshifts of $z = 2.0$ and $z = 6.6$. All images have been generated with a low-level Gaussian noise to simulate real observing conditions and with a seeing FWHM of $0.1''$ corresponding to that measured of HST WFC3/UVIS and ACS/WFC images. The original images of the GCs today were reproduced by populating the mass function up to the MSTO mass derived for each cluster in order to confirm that the generated results matched the original data and that we could recover this data from our images using SExtractor.

Presented in Figure 19 are the 4000×4000 RGB HST images of each GC in the sample as it would have appeared when it had just formed with all stars still present on the main-sequence. The images have been generated using the methods outlined previously and sizes according to the half-mass radii taken from [Harris \(1996\)](#) assuming a Gaussian distribution of stars. The filters used are R: F814W, G: F606W and B: F438W, using a linear scale from the publicly available code img_scale.py ([Shin, 2016](#)).

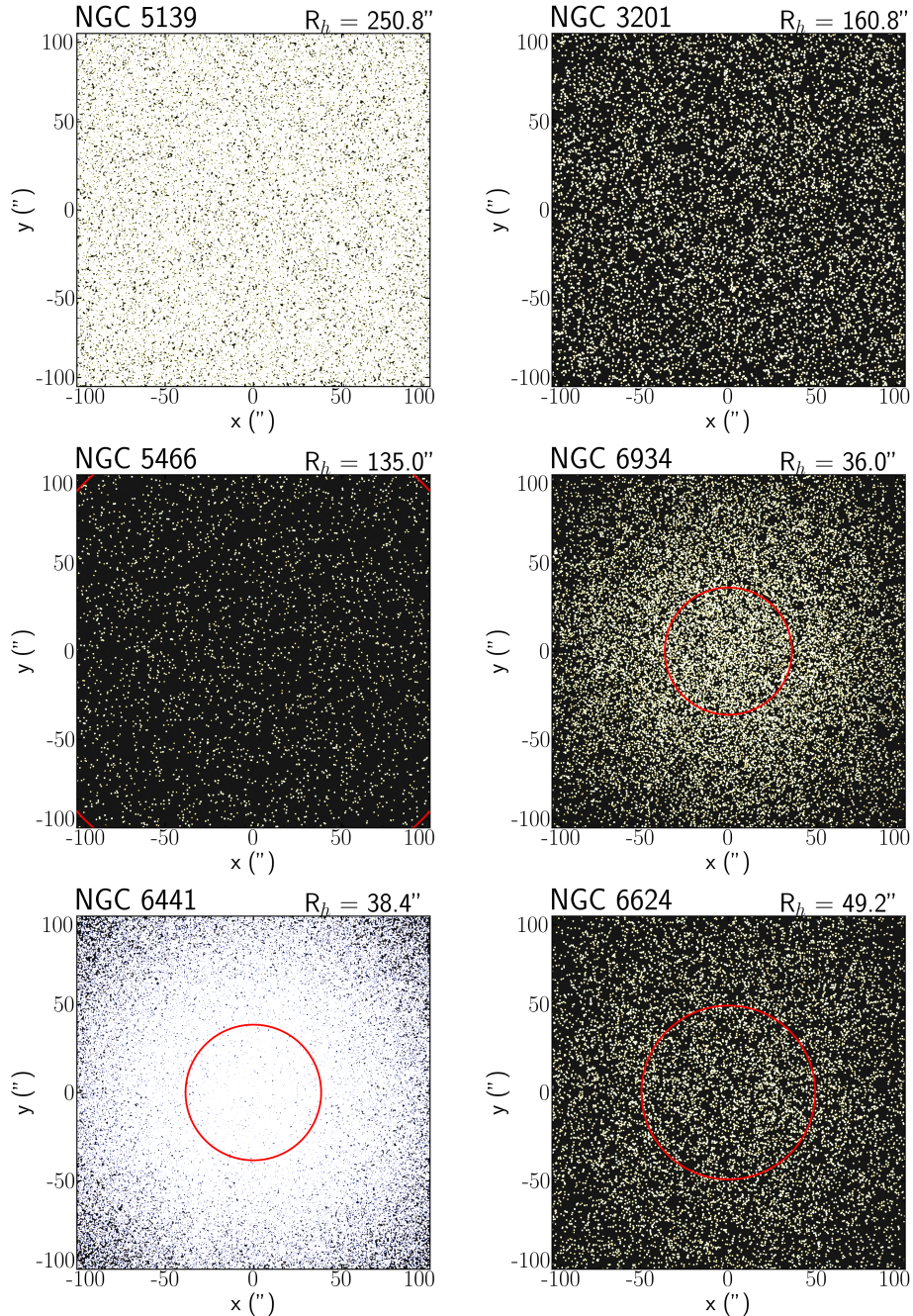


Figure 19: Generated young Milky Way globular clusters as they would appear at the distances they are at today in the galaxy, derived from fitting isochrones previously in Section 4. These RGB images have been created using a linear scale and filters R: F814W, G: F606W and B: F438W, with a cut of -0.005 to $+0.05$ counts s^{-1} . The red circle shows the half-mass radius, R_h , of the cluster used in this modelling, taken from [Harris \(1996\)](#). The image of young NGC 5139 is of the extremely dense core, hence the difference in appearance.

NGC 6441 is one of the GCs in the sample with a small enough half-mass radius, at the distance it is at in the Milky Way, to be viewed in entirety within one single HST frame. It is also the second most massive of those in the sample and the differences between it and e.g. NGC 6934, with a similar half-mass radius, can be seen clearly in Figure 19. NGC 6441 is more densely populated and significantly bluer in colour. The blue colour arises from the massive O and B type stars that are more numerous in the higher mass clusters, with the most massive of these types of stars only present in NGC 5139 and NGC 6441 (see the IMFs, Figure 11). Figure 20 shows NGC 6441 in the three different filters used for this study, illustrating how a GC differs in appearance with filter. Despite containing high mass stars, GCs will be dominated by lower mass stars that have a spectrum which peaks in the visible, hence more stars appear in F606W and F814W.

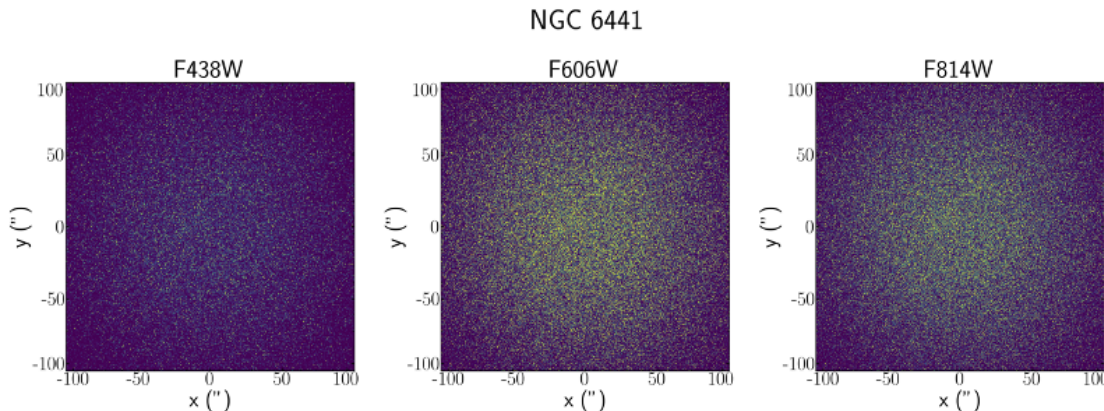


Figure 20: HST images of young NGC 6441 at a distance of 9.7 kpc as modelled and produced in this study, in filters: F438W, F606W and F814W. The 4000 x 4000 pixel images have been produced with a cut of -0.002 to +150 counts s⁻¹. More stars can be seen to be visible in the F606W and F814W images.

The six young GCs are placed at high redshifts of $z = 2.0$ and $z = 6.6$ where they appear as a compact single PSF, as discussed in Section 5.6. The magnitudes of each cluster in various filters are presented in Table 15, none of which are above the limiting magnitude of a HUDF-like exposure of $m_{AB} \sim 29$. Therefore, through our modelling of repopulating the high mass end of the mass function, not even the most massive (young NGC 5139) would be visible with a HUDF exposure. The clusters are brightest in the UV due to the peak of higher mass stars spectra in these regions, however, this is still not enough to make the clusters visible. We do see that a cluster will be fainter in the reddest filters, e.g. rest-frame F814W, but will become gradually brighter towards the UV. Increasing the number of high mass stars will likely increase the UV magnitude such that it may be observed.

Cluster	m_{F814W}		m_{F606W}		m_{F438W}		m_{UV}		m_{F475W}	m_{F110W}
	$z=2.0$	$z=6.6$	$z=2.0$	$z=6.6$	$z=2.0$	$z=6.6$	$z=2.0$	$z=6.6$	$z=2.0$	$z=6.6$
NGC 5139	34.1	37.2	33.8	36.8	33.5	36.6	33.2	36.3	33.2	36.3
NGC 3201	37.6	40.6	37.2	40.3	36.9	40.0	36.6	39.7	36.7	39.7
NGC 5466	38.8	41.8	38.5	41.5	38.3	41.3	38.0	41.0	38.1	41.0
NGC 6934	37.8	40.9	37.5	40.6	37.2	40.3	36.8	40.0	36.9	40.1
NGC 6441	35.3	38.3	34.9	38.0	34.6	37.7	34.3	37.4	34.4	37.5
NGC 6624	38.3	41.4	38.0	41.0	37.7	40.8	37.4	40.4	37.4	40.5

Table 15: Calculated magnitudes of young GCs for each original Milky Way GC in the sample as observed at high redshifts 2.0 and 6.6. All filters show rest-frame magnitudes in various filters, including a perfect UV tophat filter, apart from F475W and F110W which are examples of observed filters needed for $z = 2.0$ and $z = 6.6$ respectively to capture the rest-frame UV of the Cluster.

We calculate that for NGC 5139 to be visible with HST at $z = 2.0$ in the observed filter of F475W (rest-frame UV), it would need to be ~ 49 times more massive than it is in our model. There is discussion over the mass budget factor of GCs meaning that when they first formed they could be up to 10 times more massive. Our model predicts that they were only 1.5 times more massive, but we are not modelling many processes such as evaporation. In reality, these young clusters will have been more massive if we take into account all processes of mass loss, but it does not seem reasonable for a factor of 49 to be possible. Therefore, we do not believe we would be able to observe young globular clusters that would go onto evolve into Milky Way globular clusters with HST, at least without the aid of phenomenon such as gravitational lensing. However, JWST will be able to observe down to much fainter magnitudes and should, in theory, be able to capture observations of these forming GCs across redshift, significantly advancing this field.

Figure 21 shows images of a young NGC 5139 placed at both $z = 2.0$ and $z = 6.6$ using the magnitudes obtained in this study for the observational filters that correspond to the rest-frame UV. While we are currently unable to observe deep enough with HST to produce these observations, if we could perform significantly longer exposures then this is how a young NGC 5139 would appear, according to our models. These images have been produced with a very low level Gaussian noise, although in reality possible observations will be of lower quality. Globular clusters at high redshift appear as a single compact source, with individual stars unable to be detected and therefore the science that can be done is limited, highlighting the importance of combining what can be learnt from Milky Way GCs with those forming in the Early Universe.

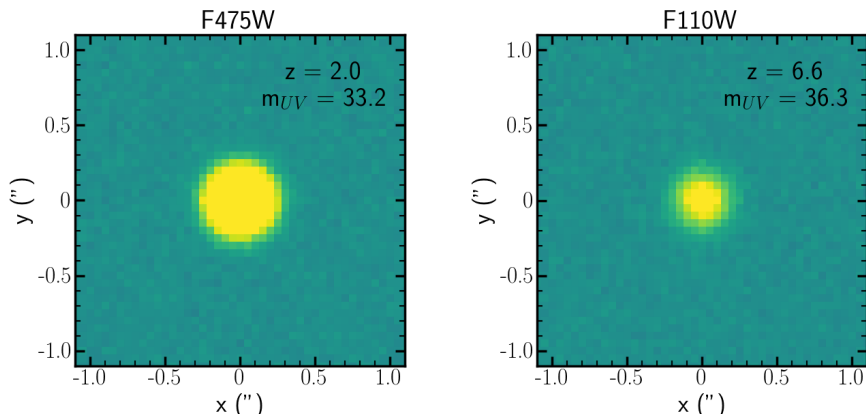


Figure 21: Young NGC 5139 modelled in this study and placed at a redshift of 2.0 and 6.6. These images have been generated using the magnitudes in the observational filters needed to capture the rest-frame UV at those redshifts, and with a cut of $\pm 3 \times 10^{-6}$ counts s^{-1} .

It is possible that globular clusters formed from giant molecular clouds that sub-fragment to produce several clusters (e.g. see [Murray & Lin, 1990](#); [Clark et al., 2005](#); [Howard et al., 2018](#)). This means that one cloud could have formed a handful of Milky Way globular clusters and the scales at high redshift, when they formed, means that they would all appear as a single PSF. Since we would not be able to resolve individual clusters, we would see the sum of all as one single compact source. Therefore we estimate the magnitude of the sum of all six young Milky Way GCs in order to investigate if this would be observable. We measure the sum of all six young GCs to have a UV rest-frame magnitude, m_{UV} , of 32.8 which is still too faint to be detected with HST. Although this is at maximum 6 times brighter than NGC 5139 on its own, if we take the upper limit of the mass budget factor to be 10 times more massive at formation and predict that 6 massive clusters like NGC 5139 or NGC 6441 formed out of one cloud then we would observe a source that is of the order of ~ 50 times more massive than NGC 5139 in our models, and therefore a source with a magnitude brighter than the limiting magnitude of ~ 29 .

7 Discussion

There are several caveats of our choice of modelling that should be highlighted and improved upon in the future. Firstly, with regards to the first section of this project, we make the assumption that the globular clusters can be represented by a single isochrone corresponding to a simple stellar population. In reality, this is known not to be true for Milky Way GCs which today appear to be made up of only one third of the original generation of stars that formed with the cluster itself. An improvement would be to attempt to identify the multiple populations in our clusters and identify the properties of the first generation of stars. Then backwards model with this single population to study how the GC appeared in the early stages, before any successive burst of star formation. This is difficult to model, hence our simplified assumption, but see, e.g. [Charbonnel et al. \(2014\)](#); [Carretta et al. \(2010\)](#) for research into identifying this first generation of stars in GCs.

Although we are unable to resolve the multiple populations in our clusters, we can infer them indirectly from the width of the main-sequences seen in Section 4. The number of isochrones within 1σ of the best-fit can be seen to increase with the width of the main-sequence; NGC 5466 has the narrowest main-sequence with 1,117 isochrones within 1σ , NGC 3201 has an intermediate main-sequence width with 4,636 isochrones within 1σ , and NGC 5139 has the widest main-sequence³ with 5,342 isochrones within 1σ . This suggests that the narrower the main-sequence, the more tightly constrained the property estimates are and the closer the GC is to a simple stellar population. Therefore the width of the main-sequence can be said to correlate with the number of best-fit isochrones and the spread of populations within the cluster. Results from NGC 6934 do not correlate with this, as it has a narrow main-sequence but the largest number of best-fit isochrones, 8,761. This is likely due to the lower quality of data which was clipped visually and subjectively.

In Section 3.1.2 we present our first CMD of the study for the most massive Milky Way GC, NGC 5139, see Figure 4. From this CMD we are able to identify a potential blue straggler population in our cluster. We find a relatively large number of 318 potential blue stragglers, compared with [Baldwin et al. \(2016\)](#) who identify 73 blue stragglers in NGC 5139. This population is identified from the position in the CMD, however, upon further inspection, we are unable to distinguish, in our case, between a blue straggler or horizontal branch population (e.g. see [Fusi Pecci et al., 1992](#), for tests on determining between the two). Horizontal branch stars, the hottest named blue hook stars, have been previously identified in the core of NGC 5139 (e.g. see [Moehler et al., 2011](#)).

As for the second section of this report there are several areas that could be improved upon in the future. We are unable to observe the young globular clusters at high redshift with HST, but this result could be different with changes to the modelling. Firstly, a top-heavy IMF e.g. [Chabrier \(2003\)](#) would significantly increase the higher mass stars that dominate the luminosity from a stellar cluster, especially in the UV. In this study, we assumed a simple [Salpeter \(1955\)](#) slope, however, investigating the different forms and how this changes our results would be a good next step. For example, adopting the observed present-day mass function slope for NGC 5139 of $\alpha = -1.2$ from [Webb & Leigh \(2015\)](#) we find that young NGC 5139 in our model would have a UV magnitude of 28.1 at $z = 2.0$ and thus is observable with a HUDF exposure. This is the case if we simply extrapolate the present-day mass function to high masses with the same slope, but in reality it is thought that the slope is steeper at high mass otherwise young GCs would have dissolved and not survived until today. We have assumed that the present-day mass function reflects the IMF, having only lost the high mass stars due to stellar evolution processes. This is a big assumption as many other dynamical processes such as mass segregation and evaporation likely cause the mass function to evolve over the clusters lifetime (see e.g. [McLaughlin & Fall, 2008](#); [Ebrahimi et al., 2020](#)).

³The width of the bins for NGC 5139 have been set with sigma clipping and is, therefore, more subjective as it is based upon the choice in the number of iterations, compared with NGC 5466 and NGC 3201 where it was not needed.

When placing the generated stars in the images, we obtain the position from a probability distribution set by the half-mass radius of the cluster from [Harris \(1996\)](#). In order to do this, we assume that the cluster can be modelled as a Gaussian distribution with half of the total number of stars contained within the half-mass radius. This relies on the assumption that the stars of different masses are uniformly distributed throughout the cluster. However, it is known that clusters over their life sort themselves according to mass, with high mass stars located in the central regions, due to a process named mass segregation. Young GCs may have stars randomly distributed because mass segregation occurs as the cluster evolves, however, it should be included in the backward modelling from today's GCs. The same Gaussian distribution of stars and half-mass radius is assumed for both x and y dimensions, relying on the idea that GCs are spherical systems of stars. In reality, many Milky Way globular clusters have been observed to be flattened caused by for example the rotation (e.g. see [Bianchini et al., 2013](#), for the flattening of NGC 5139). The majority of young GCs generated in this study are either at high z where the cluster appears as a point source or of the cores of clusters (see Figure 19) in which case the flattening will not be important. However, for those where we generate the entire cluster, e.g. NGC 6934 in Figure 19, the flattening could be more important in changing how the cluster appears. In order to incorporate this into the models, information would be needed on the direction of the flattening, and we would require kinematics to be able to measure this, which is beyond the scope of this study.

All of the modelling assumes that the physical size of the half-mass radius for the young GC is the same as that observed today, which is not correct as they will have been more extended when they first formed. As well as GCs being more extended when they were younger, they were also more massive. In our model, we repopulate the high mass end of the mass function in order to obtain the mass of our young GC. This is only accounting for high mass stars lost from the cluster as they end their life due to stellar evolution. However, as mentioned previously, there are other mechanisms by which stars are thought to be lost from a cluster over its lifetime. A significant amount of low mass stars are likely lost due to evaporation as a result of the low escape velocities of these systems. This means using the present-day mass function of our Milky Way GCs we are missing a significant number of low mass stars and therefore underestimating the normalisation, thus also underestimating the number of high mass stars. Our models suggest that young GCs were ~ 1.5 times more massive than they are today, in agreement with [Pozzetti et al. \(2019\)](#) who say that a factor of ~ 1.7 likely accounts for the mass loss due to stellar evolution. However, it is more likely a factor of $\sim 4\text{-}10$ when taking into account all other processes ([Webb & Leigh, 2015](#)).

Our scalings of the young GCs as they appear in the Milky Way, see Figure 19, do not quite match up with that of the original HST data. Our generated images reflect the modelling of the fraction of the cluster that should be seen, using the specified pixel scale, distance to the cluster and Gaussian distribution set by the half-mass radius, shown in Figure 14. This may be improved by instead using the smaller half-light radius of the clusters to scale the size in the generated images.

As well as improving the modelling by taking into account all of the caveats outlined here, more could be done in the future to further the science of this work. It would be interesting to investigate the different origins of the Milky Way GCs in our sample. According to [Forbes \(2020\)](#) both NGC 6441 and NGC 6624 likely formed with the galaxy itself, whereas NGC 5139, NGC 3201 and NGC 5466 are thought to have formed in a dwarf galaxy named Sequoia and later accreted into the Milky Way. NGC 6934 is also thought to have been accreted, but an original progenitor galaxy has not yet been identified. It would be worth investigating any differences we observe that line up with these different origins. NGC 5139 is in-fact thought to have been the nuclear cluster of Sequoia before being accreted into our galaxy as a globular cluster; therefore, differences are likely present if this origin is correct. It would also be interesting to extend this study by looking into whether young globular clusters could have contributed to reionisation and attempts could be made to quantify this. Finally, if we can observe with JWST, we will be able to witness young and forming GCs. Thus it is important to prepare what science can be done with these observations.

8 Summary

Archival Hubble Space Telescope (HST) data for six Milky Way globular clusters from the various locations in our galaxy, including the bulge and halo, combined with Dartmouth stellar isochrones from Dotter et al. (2008) have allowed us to successfully measure the properties, including both ages and metallicities, of these Galactic GCs. These have been coupled with stellar evolution models to repopulate the Salpeter (1955) IMF identifying how these clusters looked in the first few Myrs after formation, when all stars remained on the main sequence. Images have been generated of these young globular clusters and magnitudes measured in various filters at redshifts 2.0 and 6.6, spanning the epoch of the Universe when these systems likely formed. The main results of this study are summarised below.

- We produce stellar catalogues of six Milky Way globular clusters from archival HST WFC3 /UVIS and ACS/WFC data in F438W, F606W and F814W. These catalogues are used to produce a CMD for each cluster from which the age, metallicity, extinction and distance were determined through fitting of Dotter et al. (2008) stellar isochrones. This is done successfully for four clusters; NGC 5139, NGC 3201, NGC 5466 and NGC 6934. We obtain age estimates between 10.5 - 12.5 Gyrs and metallicity estimates of $[Fe/H] = -1.6$ dex to $[Fe/H] = -2.2$ dex, with typical uncertainties of ± 2.0 Gyrs and ± 0.5 dex respectively. For the bulge GCs, NGC 6441 and NGC 6624, we were unsuccessful in producing a CMD and so literature values for the properties were used.
- Ages derived for each of the Milky Way GCs were used to calculate the MSTO masses that were all found to be $\sim 1 M_{\odot}$. The present day mass functions were produced using the total dynamical mass of the GCs taken from Baumgardt & Hilker (2018) and accounting for the contributions from main sequence stars and white dwarf remnants in the cluster to calculate the normalisation factor of the mass function with an assumed Salpeter (1955) slope.
- Initial mass functions were derived assuming the same slope and form as present day and repopulating the high mass stars up to $120 M_{\odot}$. These were used for generating stars of a given mass according to the IMF and models were assumed to derive the temperature and luminosity of the star, in order to calculate a radius. Fluxes and magnitudes for each generated star were produced by using the black-body spectrum for a star of specific temperature convolved through the different filters.
- We generate the six Milky Way globular clusters as they would have appeared when they were younger. The magnitudes of these clusters placed at $z = 2.0$ and $z = 6.6$ are presented in the rest frame filters F438W, F606W, F814W and a perfect UV filter, along with the observational filters, F475W and F110W, required for capturing the rest-frame UV at $z = 2.0$ and $z = 6.6$ respectively. We find that young GCs that would evolve into those seen in the Milky Way today are too faint to be observed at high redshift with HST, even in the rest-frame UV. However, this modelling does not take into account stellar loss of the cluster over its lifetime due to processes other than stellar evolution. Therefore they were likely more massive at formation than predicted in this study.

There are many improvements that could be made to our modelling in the future, as discussed in Section 7. More accurate models of how the mass function of globular clusters evolve are needed to constrain the mass of young GCs and the factor by which this has changed to today. Observations of young and forming globular clusters at high redshift will be key for constraining these models. While we believe that young GCs are too faint to be observed at high redshifts with HST, JWST on the other hand will be able to observe to much fainter magnitudes and will be able to detect many more of these progenitor GCs. The number of these progenitors that can be detected will depend on their mass and thus will constrain our estimates of this modelling and of globular cluster evolution.

References

- Aghanim N., et al., 2018, arXiv preprint arXiv:1807.06209
- Alonso-García J., Mateo M., Sen B., Banerjee M., Catelan M., Minniti D., Von Braun K., 2012, The Astronomical Journal, 143, 70
- Anderson J., et al., 2008, The Astronomical Journal, 135, 2055
- Ashman K. M., Zepf S. E., 1992, The Astrophysical Journal, 384, 50
- Ashman K. M., Zepf S. E., 2008, Globular cluster systems. Vol. 30, Cambridge University Press
- Baldwin A., Watkins L., van der Marel R., Bianchini P., Bellini A., Anderson J., 2016, The Astrophysical Journal, 827, 12
- Baumgardt H., Hilker M., 2018, Monthly Notices of the Royal Astronomical Society, 478, 1520
- Baumgardt H., De Marchi G., Kroupa P., 2008, The Astrophysical Journal, 685, 247
- Beasley M. A., 2020, arXiv, pp arXiv–2003
- Beckwith S. V., et al., 2006, The Astronomical Journal, 132, 1729
- Bedin L. R., Piotto G., Anderson J., Cassisi S., King I. R., Momany Y., Carraro G., 2004, The Astrophysical Journal Letters, 605, L125
- Bekki K., Mackey A., 2009, Monthly Notices of the Royal Astronomical Society, 394, 124
- Bellini A., et al., 2014, The Astrophysical Journal, 797, 115
- Bellini A., Anderson J., Bedin L., King I., van der Marel R., Piotto G., Cool A., 2017a, The Astrophysical Journal, 842, 6
- Bellini A., Anderson J., van der Marel R., King I., Piotto G., Bedin L., 2017b, The Astrophysical Journal, 842, 7
- Bellini A., Milone A., Anderson J., Marino A., Piotto G., van der Marel R., Bedin L., King I., 2017c, The Astrophysical Journal, 844, 164
- Bertin E., Arnouts S., 1996, , [117, 393](#)
- Bianchini P., Varri A., Bertin G., Zocchi A., 2013, The Astrophysical Journal, 772, 67
- Blumenthal G. R., Faber S., Primack J. R., Rees M. J., 1984, Nature, 311, 517
- Bournaud F., Duc P.-A., Emsellem E., 2008, Monthly Notices of the Royal Astronomical Society: Letters, 389, L8
- Bouwens R., Illingworth G., Oesch P., Maseda M., Ribeiro B., Stefanon M., Lam D., 2017, arXiv preprint arXiv:1711.02090
- Boylan-Kolchin M., 2018, Monthly Notices of the Royal Astronomical Society, 479, 332
- Bruzual A G., 2010, Philosophical Transactions of the Royal Society A: Mathematical, Physical and Engineering Sciences, 368, 783
- Calamida A., et al., 2020, The Astrophysical Journal, 891, 167
- Calzetti D., Kinney A. L., Storchi-Bergmann T., 1994, The astrophysical journal. Chicago. Vol. 429, no. 2, pt. 1 (July 1994), p. 582-601

- Carretta E., Bragaglia A., Gratton R., D’Orazi V., Lucatello S., 2009, *Astronomy & Astrophysics*, 508, 695
- Carretta E., Bragaglia A., Gratton R. G., Recio-Blanco A., Lucatello S., D’Orazi V., Cassisi S., 2010, *Astronomy & Astrophysics*, 516, A55
- Carriere J., Horowitz C., Piekarewicz J., 2003, *The Astrophysical Journal*, 593, 463
- Chaboyer B., 2001, in *Astrophysical Ages and Times Scales*. p. 162
- Chabrier G., 2003, *Publications of the Astronomical Society of the Pacific*, 115, 763
- Charbonnel C., Chantereau W., Krause M., Primas F., Wang Y., 2014, *Astronomy & Astrophysics*, 569, L6
- Clark P. C., Bonnell I. A., Zinnecker H., Bate M. R., 2005, *Monthly Notices of the Royal Astronomical Society*, 359, 809
- Clement C. M., et al., 2001, *The Astronomical Journal*, 122, 2587
- Contenta F., Varri A. L., Heggie D. C., 2015, *Monthly Notices of the Royal Astronomical Society: Letters*, 449, L100
- Davies M. B., Piotto G., Angeli F. D., 2004, *Monthly Notices of the Royal Astronomical Society*, 349, 129
- De Marchi G., et al., 2004, *Instrument Science Report*, (STScI, Baltimore)
- Dotter A., Chaboyer B., Jevremović D., Baron E., Ferguson J. W., Sarajedini A., Anderson J., 2007, *The Astronomical Journal*, 134, 376
- Dotter A., Chaboyer B., Jevremović D., Kostov V., Baron E., Ferguson J. W., 2008, *The Astrophysical Journal Supplement Series*, 178, 89
- Ebrahimi H., Sollima A., Haggi H., Baumgardt H., Hilker M., 2020, arXiv preprint arXiv:2004.02906
- Eker Z., et al., 2015, *The Astronomical Journal*, 149, 131
- Fall S. M., Rees M. J., 1988, in *Symposium-International Astronomical Union*. pp 323–332
- Forbes D. A., 2020, *Monthly Notices of the Royal Astronomical Society*, 493, 847
- Fryer C. L., 2004, *The Astrophysical Journal Letters*, 601, L175
- Fusi Pecci F., Ferraro F., Corsi C., Cacciari C., Buonanno R., 1992, *The Astronomical Journal*, 104, 1831
- Giesers B., et al., 2018, *Monthly Notices of the Royal Astronomical Society: Letters*, 475, L15
- Gnedin O. Y., Zhao H., Pringle J., Fall S. M., Livio M., Meylan G., 2002, *The Astrophysical Journal Letters*, 568, L23
- Goldsbury R., Richer H. B., Anderson J., Dotter A., Sarajedini A., Woodley K., 2010, *The Astronomical Journal*, 140, 1830
- Gonzalez O., Rejkuba M., Zoccali M., Valenti E., Minniti D., Schultheis M., Tobar R., Chen B., 2012, *Astronomy & Astrophysics*, 543, A13
- Gratton R. G., Carretta E., Bragaglia A., 2012, *The Astronomy and Astrophysics Review*, 20, 50

- Guo Q., White S., Li C., Boylan-Kolchin M., 2010, Monthly Notices of the Royal Astronomical Society, 404, 1111
- Guth A. H., 1981, Physical Review D, 23, 347
- Habets G., Heintze J., 1981, Astronomy and Astrophysics Supplement Series, 46, 193
- Harris W. E., 1996, The Astronomical Journal, 112, 1487
- Heger A., Fryer C., Woosley S., Langer N., Hartmann D. H., 2003, The Astrophysical Journal, 591, 288
- Helmi A., 2020, arXiv preprint arXiv:2002.04340
- Hillenbrand L. A., White R. J., 2004, The Astrophysical Journal, 604, 741
- Howard C. S., Pudritz R. E., Harris W. E., 2018, Nature Astronomy, 2, 725
- Hubble E., 1929, Proceedings of the national academy of sciences, 15, 168
- Jimenez R., 1998, Proceedings of the National Academy of Sciences, 95, 13
- Kalirai J., et al., 2009, Instrument Science Report WFC3, 31
- Kaluzny J., Olech A., Stanek K., 2001, The Astronomical Journal, 121, 1533
- Kepler S. O., Kleinman S. J., Nitta A., Koester D., Castanheira B. G., Giovannini O., Costa A. F. M. d., Althaus L., 2007, Monthly Notices of the Royal Astronomical Society, 375, 1315
- Kharchenko N., Piskunov A., Schilbach E., Röser S., Scholz R.-D., 2016, Astronomy & Astrophysics, 585, A101
- Kikuchihiara S., et al., 2019, arXiv preprint arXiv:1905.06927
- Kraft R. P., 1979, Annual Review of Astronomy and Astrophysics, 17, 309
- Krauss L. M., Chaboyer B., 2003, Science, 299, 65
- Kremer K., Claire S. Y., Chatterjee S., Rodriguez C. L., Rasio F. A., 2018, The Astrophysical Journal Letters, 855, L15
- Kruijssen J. D., 2014, Classical and Quantum Gravity, 31, 244006
- Kulkarni S., Hut P., McMillan S. J., 1993, Nature, 364, 421
- Kuranov A., Postnov K., 2006, Astronomy letters, 32, 393
- Leaman R., VandenBerg D. A., Mendel J. T., 2013, Monthly Notices of the Royal Astronomical Society, 436, 122
- Lemaitre G., 1927, in Annales de la Société Scientifique de Bruxelles. pp 49–59
- Ma J., Wu Z., Wang S., Fan Z., Zhou X., Wu J., Jiang Z., Chen J., 2010, Publications of the Astronomical Society of the Pacific, 122, 1164
- Mamajek E., 2011, Effective temperature (Teff) vs. stellar mass (M/Msun) for main sequence stars, <http://www.pas.rochester.edu/~emamajek/coolplots.html>
- Marin-Franch A., et al., 2009, The Astrophysical Journal, 694, 1498
- Marino A. F., et al., 2018, The Astrophysical Journal, 859, 81

- Massari D., Koppelman H. H., Helmi A., 2019, *Astronomy & Astrophysics*, 630, L4
- Mathis J. S., 1990, *Annual Review of Astronomy and Astrophysics*, 28, 37
- McGreer I. D., Mesinger A., D'Odorico V., 2015, *Monthly Notices of the Royal Astronomical Society*, 447, 499
- McLaughlin D. E., Fall S. M., 2008, *The Astrophysical Journal*, 679, 1272
- Meftah M., et al., 2018, *Astronomy & Astrophysics*, 611, A1
- Milone A., et al., 2017, *Monthly Notices of the Royal Astronomical Society*, 464, 3636
- Moehler S., Dreizler S., Lanz T., Bono G., Sweigart A., Calamida A., Nonino M., 2011, *Astronomy & Astrophysics*, 526, A136
- Morgan W. W., Keenan P., 1973, *Annual Review of Astronomy and Astrophysics*, 11, 29
- Murray S. D., Lin D. N., 1990, *The Astrophysical Journal*, 363, 50
- Myeong G., Vasiliev E., Iorio G., Evans N., Belokurov V., 2019, *Monthly Notices of the Royal Astronomical Society*, 488, 1235
- Oey M. S., Clarke C., 2005, *The Astrophysical Journal Letters*, 620, L43
- Oser L., Ostriker J. P., Naab T., Johansson P. H., Burkert A., 2010, *The Astrophysical Journal*, 725, 2312
- O'Malley E. M., Gilligan C., Chaboyer B., 2017, *The Astrophysical Journal*, 838, 162
- Peebles P., 1982, *The Astrophysical Journal*, 263, L1
- Penzias A. A., Wilson R. W., 1965, *The Astrophysical Journal*, 142, 419
- Peterson C. J., 1987, *Publications of the Astronomical Society of the Pacific*, 99, 1153
- Phipps F., Khochfar S., Varri A. L., Vecchia C. D., 2019, arXiv preprint arXiv:1910.09924
- Piotto G., 2013, HST Proposal
- Piotto G., Zoccali M., King I., Djorgovski S., Sosin C., Dorman B., Rich R., Meylan G., 1999, *The Astronomical Journal*, 117, 264
- Piotto G., et al., 2004, *The Astrophysical Journal Letters*, 604, L109
- Piotto G., et al., 2012, *The Astrophysical Journal*, 760, 39
- Piotto G., et al., 2015, *The Astronomical Journal*, 149, 91
- Pozzetti L., Maraston C., Renzini A., 2019, *Monthly Notices of the Royal Astronomical Society*, 485, 5861
- Raso S., Ferraro F., Dalessandro E., Lanzoni B., Nardiello D., Bellini A., Vesperini E., 2017, *The Astrophysical Journal*, 839, 64
- Recio-Blanco A., Aparicio A., Piotto G., De Angeli F., Djorgovski S., 2006, *Astronomy & Astrophysics*, 452, 875
- Renzini A., 2017, *Monthly Notices of the Royal Astronomical Society: Letters*, 469, L63

- Richer H. B., Fahlman G. G., Buonanno R., Fusi Pecci F., Searle L., Thompson I. B., 1991, The Astrophysical Journal, 381, 147
- Rodrigo C., Solano E., 2013, Technical report, Filter Profile Service Access Protocol. Version 1.0. IVOA Note 2013 May 10
- Rodrigo C., Solano E., Bayo A., 2012, IVOA Working Draft, 15
- STScI 2019, Wide Field Camera 3, HST Instrument Handbook
- STScI 2020, ACS Zero-Point Calculator, <https://acszeropoints.stsci.edu>
- Sabbi E., 2009, HST Proposal
- Salpeter E. E., 1955, The Astrophysical Journal, 121, 161
- Sandage A. R., 1953, The Astronomical Journal, 58, 61
- Sandage A., 1970, The Astrophysical Journal, 162, 841
- Sarajedini A., 2005, HST Proposal
- Sarajedini A., et al., 2006, arXiv preprint astro-ph/0612598
- Shin M., 2016, Python code to convert FITS files to images, https://astromsshin.github.io/science/code/Python_fits_image/index.html
- Smith R., 1983, The Observatory, 103, 29
- Smith G. H., Wood P. R., Faulkner D., Wright A. E., 1990, The Astrophysical Journal, 353, 168
- Sobral D., Matthee J., Darvish B., Schaerer D., Mobasher B., Röttgering H. J., Santos S., Hemmati S., 2015, The Astrophysical Journal, 808, 139
- Sobral D., et al., 2019, Monthly Notices of the Royal Astronomical Society, 482, 2422
- Steiner A. W., Heinke C. O., Bogdanov S., Li C. K., Ho W. C., Bahramian A., Han S., 2018, Monthly Notices of the Royal Astronomical Society, 476, 421
- Steinmetz M., Navarro J. F., 2002, New Astronomy, 7, 155
- Stetson P. B., VandenBerg D. A., Bolte M., 1996, Publications of the Astronomical Society of the Pacific, 108, 560
- Straka W. C., 1971, The Astrophysical Journal, 165, 109
- Suzuki N., Fukugita M., 2018, The Astronomical Journal, 156, 219
- Taylor M. B., 2005, in Astronomical data analysis software and systems XIV. p. 29
- Toomre A., Tinsley B., Larson R., 1977, in Proceedings of a Conference at Yale University, May. pp 19–21
- VandenBerg D. A., Brogaard K., Leaman R., Casagrande L., 2013, The Astrophysical Journal, 775, 134
- Vanzella E., et al., 2017, Monthly Notices of the Royal Astronomical Society, 467, 4304
- Ventura P., D'Antona F., Mazzitelli I., Gratton R., 2001, The Astrophysical Journal Letters, 550, L65

- Webb J. J., Leigh N. W., 2015, Monthly Notices of the Royal Astronomical Society, 453, 3278
- Weidemann V., Koester D., 1983, Astronomy and Astrophysics, 121, 77
- Willmer C. N., 2018, The Astrophysical Journal Supplement Series, 236, 47
- Windhorst R. A., et al., 2011, The Astrophysical Journal Supplement Series, 193, 27
- Woo J.-H., Urry C. M., 2002, The Astrophysical Journal, 579, 530
- Wright E. L., 2006, Publications of the Astronomical Society of the Pacific, 118, 1711
- Zinn R., 1996, in Formation of the Galactic Halo... Inside and Out. p. 211